AAEC/E374

AAEC/E374

AUSTRALIAN ATOMIC ENERGY COMMISSION

RESEARCH ESTABLISHMENT

LUCAS HEIGHTS

TRANSMISSION ELECTRON MICROSCOPE PROCEDURES FOR CHARACTERISING DISLOCATION LOOPS IN NEUTRON-IRRADIATED ZIRCONIUM AND ITS ALLOYS

by

R.G. BLAKE
A. JOSTSONS
P.M. KELLY

April 1976

ISBN O 642 99745 4

AUSTRALIAN ATOMIC ENERGY COMMISSION

RESEARCH ESTABLISHMENT

LUCAS HEIGHTS

TRANSMISSION ELECTRON MICROSCOPE PROCEDURES FOR CHARACTERISING DISLOCATION LOOPS IN NEUTRON-IRRADIATED ZIRCONIUM AND ITS ALLOYS

by

R.G. BLAKE

A. JOSTSONS

P.M. KELLY

ABSTRACT

Complete characterisation of the dislocation loops in irradiated zirconium and its alloys presents particular problems; these include unfavourable texture, the presence of thin foil artefacts, the non-edge character of the loops and their elliptical shape. The procedures adopted to deal with these problems are described and a number of precautionary measures are listed. After considering the possible confusion between thin foil artefacts and small defect clusters, the report outlines the characterisation procedure in the order: Burgers vector identification; loop geometry; loop nature; and quantitative measurements. A detailed analysis of the possible errors associated with loop ellipticity is given in Appendix A.

National Library of Australia card number and ISBN 0 642 99745 4

The following descriptors have been selected from the INIS Thesaurus to describe the subject content of this report for information retrieval purposes. For further details please refer to IAEA-INIS-12 (INIS: Manual for Indexing) and IAEA-INIS-13 (INIS: Thesaurus) published in Vienna by the International Atomic Energy Agency.

BURGERS VECTOR; DISLOCATIONS; ELECTRON MICROSCOPY; ELLIPTICAL CONFIGURATION; ERRORS; IRRADIATION; MANUALS; MEASURING METHODS; NEUTRONS; PHYSICAL RADIATION EFFECTS; RECOMMENDATIONS; ZIRCONIUM; ZIRCONIUM BASE ALLOYS

CONTENTS

Figure 12	Average values of loop ellipticity for the loops shown in Figure 11. The numbers in brackets represent the number of loops averaged in each size interval
Figure 13	Kikuchi map, as seen on the microscope screen, showing the sense of $\underline{g} = \pm(11\bar{2}\bar{2})$ for loop characterisation near the safe orientation $[11\bar{2}3]$
Figure 14	Same field as Figure 6, but with $\underline{z} \approx [1\bar{2}13]$
Figure 15	Same field as Figures 6 and 14, but with $\underline{z} \approx [2\bar{1}\bar{1}3]$
Figure 16	Size distribution plots for 261 loops in one area of a foil of zirconium irradiated at 668 K (395°C) to 6.4×10^{23} neutrons m^{-2} (> 1 MeV)
Figure 17	Size distribution plot for 426 loops taken from the same specimen used for Figure 16, but from another grain
APPENDIX A	The Effect of Loop Ellipticity on the Accuracy of Loop Normal Determinations from Trace Analysis in Thin Foils
APPENDIX B	Nomenclature

1. INTRODUCTION

Compared to other materials such as Cu, Au, Al and Mo, the characterisation of dislocation loops in neutron-irradiated zirconium and its alloys has received little attention. In fact, there are only seven papers in which any attempt has been made to identify the Burgers vector of the loops (Riley & Grundy 1972; Kelly & Blake 1973a; Adamson et al. 1974; Northwood & Gilbert 1974; Blake et al. 1974; Northwood 1975; Gilbert 1975), and in only three of these has the nature of the loops been determined (Kelly & Blake 1973a; Blake et al. 1974; Gilbert 1975). These numbers can be increased if ion and electron induced damage are included (Gulden & Bernstein 1966; Gelles & Harbottle 1974).

The other characteristic of the published work on radiation damage in zirconium is the controversy which still surrounds the existence of dislocation loops with a $\underline{c}$ component in their Burgers vector*. The situation, as outlined in a recent review by Madden (1974) and in subsequent work, is as follows. Kelly & Blake (1973a), Blake et al. (1974), Northwood & Gilbert (1974), Northwood (1975) and Gilbert (1975) all failed to find any evidence for loops with a Burgers vector other than $a/3\ \langle 11\bar{2}0\rangle$. Gulden & Bernstein (1966) obtained similar results in their examination of Kr ion-bombarded zirconium. On the other hand, Riley & Grundy (1972) and Adamson et al. (1973) concluded that at least some of the loops had a Burgers vector which included a $\underline{c}$ component. This was supported by the work of Gelles & Harbottle (1974) on electron-irradiated zirconium and Lee & Koch (1974) on Ni ion bombardment. Bell's (1975) conclusion that 'corduroy' contrast is associated with $\underline{c}$ component damage also supports this view, although more recent work (Kelly et al. 1975) indicates that corduroy is not caused by $\underline{c}$ component damage.

The shortage of published results on radiation damage in zirconium, and the apparent Burgers vector controversy, are both probably the direct result of the numerous difficulties associated with the analysis of dislocation loops in irradiated zirconium using transmission electron microscopy. These difficulties arise from a variety of sources: the unfavourable texture of many zirconium alloy specimens; the non-edge character of the loops; the ellipticity of the loops; and the presence of thin foil artefacts such as surface oxide and hydrides.

This report identifies these problem areas, describes procedures for dealing with them and lists a number of precautionary measures which must be adopted to achieve a successful characterisation of the dislocation loops in irradiated zirconium. The analysis procedure is illustrated mainly with reference to thin foils made from zirconium samples irradiated at 668 K (395°C) to a fast neutron fluence in the range 2×10^{23} to 2×10^{24} neutrons m^{-2} ($E > 1$ MeV).

Although the results apply to these particular irradiation conditions only and, quite naturally, support the authors' earlier conclusion that there are no $\underline{c}$ component loops, the procedures they illustrate are quite general and should apply to <u>any</u> sample of irradiated zirconium that contains resolvable loops. This is particularly true of the possible sources of error and the precautionary measures that must be adopted to avoid these pitfalls. In fact, the particular sample chosen as an example is less affected by some of the

---

* See Appendix B for definition of symbols used.

problems that arise than are the specimens irradiated at lower temperatures or to higher doses. If this report succeeds in encouraging others to work on radiation damage in zirconium alloys and eventually leads, one way or the other, to a complete settlement of the Burgers vector controversy, then it will have served its purpose.

2. EXPERIMENTAL DETAILS

Zone-refined zirconium was cold rolled to strips 0.25 mm thick, annealed in vacuum for one hour at 1073 K (800°C), and then irradiated in a high temperature rig located in the hollow fuel element positions of the reactor HIFAR. After irradiation, 3 mm diameter discs were spark-machined from the strips and thin foils prepared by electrolytic jet polishing.

Thin foils were examined either at 100 kV in a JEM 7A electron microscope fitted with a ± 30° tilt goniometer stage and, where necessary, using a cartridge in which the specimen is inclined at 40° to give orientations of up to 70° to the specimen normal (Blake et al. 1972), or at 200 kV in a JSEM-200 fitted with a ± 45° double-tilt goniometer stage that had been modified to give ± 50° tilt about one axis.

The ability to tilt specimens to large angles is essential if a thorough analysis is to be carried out. The pronounced texture in zirconium sheet or tubing specimens is both a blessing and a bane to electron microscopists. In most samples of sheet or tubing the $\underset{\sim}{c}$ axis is inclined at about 30 to 40° to the specimen normal. This means that, with a limited tilt goniometer stage ($\leqslant 30°$), it is not possible to tilt any given grain into a prism orientation and even the basal orientation may be difficult to obtain on occasions. Admittedly there will be a few 'renegade' grains that do not follow the normal texture, particularly in fine grained material. These grains may by chance be oriented so that a prism direction is almost normal to the specimen. Although such grains provide easy access to the prism orientation, it will be absolutely impossible to tilt them into the basal orientation.

To conduct a really thorough investigation of the dislocation loops in a given area, micrographs should be taken over as much of a standard stereographic triangle as possible and so should include the basal and one of the prism orientations. For such experiments, the standard zirconium texture, which is anathema to those microscopists provided only with a low tilt stage, becomes a blessing to their more fortunate brethren and permits both prism and basal orientations to be achieved with a ± 50° tilt range. Hence, the ideal microscope stage for work on zirconium should possess this large range of tilt together with the stability and fine movement required to set up specific diffracting conditions at any given orientation.

3. LOOP CHARACTERISATION PROCEDURE

This will be discussed by first considering possible sources of error that could arise from mistaking thin foil artefacts for radiation damage and then outlining the characterisation procedure in the order: Burgers vector identification; loop geometry; loop nature; and quantitative measurements.

3.1 Artefacts in Thin Foil Images of Zirconium

The majority of electron microscopists with extensive experience of zirconium and its alloys recognise the existence of two main artefacts in thin foils of zirconium — hydrides and surface oxide. Each of these artefacts is introduced during electropolishing and can sometimes produce images which may be mistakenly interpreted as due to small defect clusters. It is therefore essential to be able to distinguish between true defect cluster contrast and these two types of artefact.

The possibility of confusing small surface hydrides with radiation damage has been recognised by Bedford & Miller (1972) and Northwood & Gilbert (1973). The latter authors conclude that it is easy to distinguish between hydrides and true damage clusters, usually because the hydrides are much larger than the 'black spot' damage produced at moderate to low irradiation temperatures. For hydrides greater than 50 nm in length, this is certainly true and the contrast from such hydrides is easily recognised (see Figure 1). When imaged with $\underline{g}$ = (0002), surface hydrides give rise to anomalous black/white strain contrast images of the type described by Rühle (1969). Examples of this are shown in Figures 1(a) and 1(b). Because one of the major strain components of these hydrides is along [0001] (Carpenter 1973), the (0002) reflection gives the most pronounced hydride contrast. When hydrides in the range 15 to 50 nm are imaged in (0002) with a small value of ω, these anomalous strain contrast images consist of double lines with a black 'tail' on one side of the image (Figure 1(a)). On reversing the sign of $\underline{g}$, the 'tail' reverses contrast (Figure 1(b)). Dislocation loops do <u>NOT</u> show this type of contrast but give characteristic double-arc images that change from outside to inside contrast with a reversal of $\underline{g}$. Hence, the presence of the black or white anomalous strain contrast 'tails' in a pair of ± (0002) micrographs is sufficient to identify the surface hydrides and distinguish them from dislocation loops.

If very small surface hydrides are present in specimens containing dislocation loops less than 10 nm in size, the possibility of confusing hydrides and loop images increases. In this size range, both features would give similar anomalous black/white images. Luckily it is extremely rare for such small hydrides to form in a foil; the background contrast from the surface oxide turns out to be a much greater source of possible confusion, as discussed later in this section. In the unlikely event that small hydrides did form in a foil containing small damage clusters, the obvious presence of larger hydrides would act as a warning signal.

Two experiments could be performed to check whether small black/white images in (0002) were caused by loops or hydrides. Both of these experimental checks rely on the fact that the hydrides are confined to the foil surface, while neutron-induced radiation damage should be distributed evenly throughout the foil. The first method uses stereo pairs under kinematic conditions with the same $\underline{g}$ to establish whether the suspect images are confined to the surface or not. The other method examines dark field images taken under dynamic conditions to see whether the black/white contrast always pointed in the same direction or not. Defect clusters distributed through the foil thickness should show the oscillation of the direction of the black/white image sense with depth as described by Rühle (1969). This should apply regardless of whether the defect clusters are all of the same type or not, since it is inconceivable that all the vacancy loops would occur in the first layer (0 to 0.3 ξ_g) and all the interstitials in the next layer (0.4 to 0.75 ξ_g) or vice versa. If the dynamic (0002) dark fields show black/white images pointing in the same direction, then the features responsible for these images must be within 0.3 ξ_g of either surface of the foil. If the sense of the black/white image contrast also turned out to be consistent with a dilatational (i.e. interstitial) strain field, then these images would almost certainly be due to hydrides and not radiation damage clusters.

Although experience in this laboratory supports the Northwood & Gilbert (1973) conclusion that hydrides are easily distinguished from dislocation loops, and indicates that very small hydrides (< 10 to 15 nm) are very rare, there is some tentative evidence to suggest that small hydrides can decorate dislocation loops near the foil surface. This is analogous to the observation that hydrides will form along the line of intersection of a grain boundary and the foil surface. If decoration of loops by hydrides does occur, the resulting contrast effects would be both complicated and confusing. Luckily such effects would be confined to very narrow layers near either surface and so would only affect a small proportion of the loops in a moderately thick foil.

The ever-present surface oxide invariably consists of small particles which can also be confused with 'black spot' images of defect clusters less than 10 nm in size (see Figures 2 (a,b)). This is potentially a more dangerous situation than the presence of hydrides. In certain cases, the oxide will give rise to additional spots on the diffraction pattern and dark field micrographs taken with such a spot will show the oxide film very clearly. An example of this is given in Figure 3, where the oxide particles appear as white spots approximately 10 nm in diameter. When such dark field micrographs can be obtained, there is no problem in recognising the presence of surface oxide and distinguishing the oxide contrast from true damage contrast.

As shown by Northwood & Gilbert (1973), oxide contrast can also be differentiated from true defect contrast by taking under- and over-focus images. Oxide particles, which are assumed to have little or no associated strain field, will change from black in an under-focus image to white in an over-focus image. This is consistent with the oxide particle image being due predominantly to phase contrast, as described by Rühle (1971) for the case of voids and bubbles. True 'black spot' defect clusters, on the other hand, give images that remain black under both extremes of focus.

Unfortunately Northwood & Gilbert's elegant technique is not universal. In the thick foils normally employed to study large loops or to avoid bent areas, there is insufficient phase contrast change with focusing position to produce a full reversal of contrast. However, their technique can still be used successfully in the thinner regions of the foil, and the suspected artefact images in the thicker regions are shown to be oxide because the density of these black spots does not change with foil thickness.

Another slight difficulty associated with the Northwood & Gilbert (1973) method stems from their assumption that the surface oxide particles have no associated strain field and therefore are almost invisible at true focus. This is obviously an oversimplification, since any surface oxide will probably be epitaxial. This will result in a small associated strain field, which should give a contrast effect that increases as ω is reduced. This ω dependent surface oxide contrast gives the mottled background structure shown in Figures 1(a,b) and 2(a,b) and reverses when the sign of $\underline{g}$ is changed. Only relatively small values of ω are possible with the $(000\bar{2})$ reflection because of the associated small extinction distance ξ_g. If the (0004) reflection is used instead of (0002), larger ω values can be obtained and the background contrast is reduced considerably (compare Figure 1(a) with Figure 1(e)). For other reflections such as $\{11\bar{2}0\}$, where the extinction distance ξ_g is also large, ω can easily be increased to the point where the background oxide contrast is reduced to a reasonable level (Figure 1(c)).

At this stage, it is worth pointing out that micrographs taken with $\underline{g}$ = (0004) rather than (0002) are particularly useful in the search for damage with a $\underline{c}$ component in its Burgers vector. The reduction in background contrast is sufficient to allow any $\underline{c}$ component damage to show up clearly. In the case of pure $\underline{a}$ loops imaged in $\{11\bar{2}0\}$ or $\{11\bar{2}2\}$, ω values between 1 and 2 are easily achieved and, in such micrographs, the dislocation loops are clearly visible against the much reduced oxide background contrast (see Figure 1(c)). Hence any $\underline{c}$ component damage (if it exists) should have a strong enough strain field to give good contrast in (0004) with ω between 0 and 2. Unfortunately, an example of this cannot be given since no $\underline{c}$ component damage has ever been observed in any of the specimens examined. The basic principle can, however, be illustrated by the observation that in (0004) micrographs the residual contrast from the a/3 $\langle 11\bar{2}0\rangle$ Burgers vector loops, which have $\underline{g}.\underline{b} = 0$, shows up clearly in the regions of the loop where $\underline{g}.\underline{b} \times \underline{u} \neq 0$ (see Figures 1(e,g)). In the (0002) micrographs with a smaller ω, this residual contrast is generally masked by the high background (see Figures 1(a,b)). This point is most important and any small ω (0002) micrograph, particularly from a specimen suspected of containing small defect clusters, *cannot* be used to prove the existence of $\underline{c}$ component damage unless it can be shown unequivocally that the observed contrast does not come from the surface oxide. Other problems associated with Burgers vector identification will be considered in the next section.

Having argued for the use of large ω micrographs to reduce the background oxide contrast, a few words of warning are appropriate. First, as Maher & Eyre (1971) have demonstrated, it is possible to obtain very weak $\underline{g}.\underline{b} = 1$ images when high order reflections are used at high ω values in areas where some of the loops satisfy the condition $\underline{g}.\underline{b} = 2$. Secondly, if ω is increased too much, there is the possibility that a 'stray' reflection can be excited and two-beam conditions are no longer obeyed. A special case of this is setting up a high positive value of ω on a reflection $\underline{g}$ and not recognising that this corresponds to a small *negative* ω for the reflection $2\underline{g}$. Normally, the intensity of the reflection $2\underline{g}$ is significantly less than that of $\underline{g}$ and a large enough value of ω can be achieved for $\underline{g}$ without reaching the point where $2\underline{g}$ makes a significant contribution. However, the $\{10\bar{1}0\}/\{20\bar{2}0\}$ reflections do *not* behave in this way. As Okamoto et al. (1967) noted, the $\{10\bar{1}0\}$ Kikuchi lines in Ag_2Al are weak and diffuse compared to the $\{20\bar{2}0\}$ Kikuchi lines.

Similar behaviour is observed in titanium (Okamoto & Thomas 1968) and in zirconium. When any attempt is made to set up diffracting conditions with a moderately large positive ω value on $\{10\bar{1}0\}$ and a small negative value of ω on $\{20\bar{2}0\}$, double images are formed (see Figure 4(a)). These double images can be avoided by setting ω positive on $\{20\bar{2}0\}$ (see Figure 4(b)). However, when using $\{20\bar{2}0\}$ care must also be taken to avoid exciting the strong $\{30\bar{3}0\}$ reflection and producing yet another double-image situation. The solution in this case is not to increase ω too much on $\{20\bar{2}0\}$. There are, therefore, two situations in zirconium when second-order reflections should be used in preference to first-order reflections. The first is the case of (0004), where this is chosen to allow large enough values of ω to be obtained, and the second is the use of $\{20\bar{2}0\}$ to avoid the double images often formed with $\{10\bar{1}0\}$.

The steps necessary to avoid confusion between thin foil artefact contrast and true damage cluster images can be summarised as follows:

(i) If very small hydrides are suspected, use kinematic stereo pairs to establish whether the images are confined to surface features. Alternatively, carry out dynamic black/white contrast experiments, as outlined by Rühle (1969), to determine both the position and the sense of the strain field surrounding the features giving the suspect images. Surface features with an interstitial strain field are almost certainly hydrides.

(ii) Use the (0004) reflection with a large ω instead of (0002), to eliminate excessive background contrast from the surface oxide film. A through focus series of micrographs, or a dark field taken with an oxide reflection, will clearly reveal the surface oxide particles.

It is worth remembering that hydride and oxide effects are also observed in *unirradiated* zirconium foils — for example see Figures 2(a,b). The extent of this artefact contrast varies from specimen to specimen and even from grain to grain in the same foil. Prolonged exposure to the electron beam can sometimes nucleate additional hydrides and will almost always enhance the oxide contrast. An example of the latter effect is shown in Figure 5. Figure 5(a) was recorded at the beginning of the examination period, and Figure 5(b) after some forty minutes in the beam. The two sets of micrographs were taken with the same $\underline{g}$ and comparable values of ω. The obvious enhancement of the background contrast during prolonged examination is attributed to contamination augmenting the oxide particle strain field. It is *not* an electron damage effect, even at 200 kV, since the electron energy is well below the displacement threshold for zirconium, which is 640 kV (Hastings et al. 1974). Finally, the time of forty minutes in the beam may seem excessive. In practice, however, times of this order are required to achieve adequate loop analysis via micrograph series taken in at least six orientations.

3.2 Burgers Vector Identification

The most rigorous method of evaluating the Burgers vector of a dislocation loop requires matching computed images with experimental images taken under a variety of diffracting conditions. This image matching technique is particularly valuable in elastically anisotropic materials, as shown by Head et al. (1973), because in such materials the usual $\underline{g}.\underline{b} = 0$ invisibility criterion can give misleading results. Fortunately, α-zirconium at ambient temperature is almost elastically isotropic with the parameters $A = 0.907$, $B = 1.149$ and $C = 1.115$ all close to unity (Fisher & Alfred 1968). Consequently, in zirconium alloys the direction of the Burgers vector can be determined by the usual invisibility criterion, which predicts that loops will be invisible or will exhibit $\underline{g}.\underline{b} \times \underline{u}$ residual contrast when $\underline{g}.\underline{b} = 0$ (Hirsch et al. 1965).

The possible Burgers vectors in hexagonal metals like zirconium, together with the reflections required to give $\underline{g}.\underline{b} = 0$ are listed by Partridge (1967). Obviously, the absence of any Burgers vector containing a $\underline{c}$ component can be established by choosing $\underline{g} = (0002)$ or (0004). Figures 6 (a,b) show an area where the operating reflection is $\underline{g} = \pm\ (2\bar{1}\bar{1}0)$ and the beam direction is approximately $[0\bar{1}10]$. The same area in a very similar orientation (but with $\underline{g} = (0002)$, see Figure 6(c)) shows that all the loops are either totally invisible or in residual contrast. This establishes that the Burgers vector does *NOT* contain any $\underline{c}$ component and that, as a consequence, the Burgers vector must be perpendicular to [0001].

Before going on to describe how the particular $\underline{a}$ type Burgers vector is established, one point must be emphasised very strongly. When using the $\underline{g}.\underline{b} = 0$ criterion, it is absolutely essential to ensure that strict two-beam conditions are obeyed. This is particularly important in the case of micrographs taken in (0002) to establish the presence or otherwise of $\underline{c}$ component damage. Working on very thin, bent foils where two-beam conditions cannot be obtained is useless, as the presence of any reflection other than (0002) will lead to contrast from pure $\underline{a}$ Burgers vector loops. This presents the difficulty that only relatively thick, flat foils can be used to establish the presence of $\underline{c}$ component Burgers vectors.

One possible check that will at least indicate that two-beam (0002) conditions are *not* being met is the presence of the forbidden (0001) reflection. This can only occur by double diffraction via a reflection of the type $\{hki\ell\}$ with ℓ odd. The presence of the double-diffracted (0001) spot therefore guarantees that two-beam conditions are *not* satisfied and renders the corresponding micrograph useless for proving the existence of $\underline{c}$ component damage. Unfortunately, the converse of this is not true and a specimen oriented so that there is no sign of the forbidden (0001) may still not satisfy two-beam conditions. All this proves is that, if another reflection is operating, it is one for which the index 1 is even. The only certain way of ensuring that two-beam conditions are met is to tilt into a position where (0002) is operative and there are *no* other Kikuchi lines near the centre spot. Reducing the camera length so that more of the pattern is visible also provides a useful check that no 'stray' reflections are operating. An example which shows the effect of departing from strict two-beam (0002) conditions is given in Figures 7(a,b).

After determining that there is no $\underline{c}$ component, other reflections must be selected to establish the exact direction of the loop Burgers vector. Figure 6(d) shows the same area as Figures 6(a-c), but it is imaged with $\underline{g} = (20\bar{2}0)$ and the beam approximately parallel to $[1\bar{2}10]$. This orientation is related to the previous one by a tilt about the [0001] axis of some 30°. In this case some, but not all, of the loops exhibit strong residual contrast characteristic of $\underline{g}.\underline{b} = 0$ and $\underline{g}.\underline{b} \times \underline{u} > 0$. This indicates that these loops have a Burgers vector of the type $a/3 \langle 11\bar{2}0\rangle$.

To complete the assignment of Burgers vectors for all the loops present, the foil was tilted about $[\bar{2}110]$ from the prism to the basal orientation. Figure 6(e) shows an intermediate foil orientation indicating that the identity of individual loops can be maintained in going through this 90° tilt whilst Figures 6(f,g) are at the basal orientation. In fact, such images were recorded more frequently during the experiment, but the micrographs are not included here. The most dramatic change in the appearance of the micrographs is the complete disappearance of the alignment that was so well defined at the prism orientations. This is merely a consequence of the overlap of adjacent (0001) bands of loops. Figures 6(h-j) show the images taken in the three $\{20\bar{2}0\}$ reflections at the basal orientation. In all cases, $\pm\underline{g}$ images were recorded but only one of each pair is shown. The loops that went out of contrast with $\underline{g} = (20\bar{2}0)$, $(\bar{2}200)$ and $(02\bar{2}0)$ must have Burgers vectors of the type $a/3\ [\bar{1}2\bar{1}0]$, $a/3\ [11\bar{2}0]$ and $a/3\ [\bar{2}110]$ respectively.

When imaged in $\{11\bar{2}0\}$ (or $\{11\bar{2}2\}$), none of the loops disappeared, but some of them (e.g. 4, 5, 13 and 14) showed weak contrast resembling $\underline{g}.\underline{b} = 0$

images. These anomalous weak images were first described in detail by Maher & Eyre (1971) who showed that they were associated with loop images for which $\underline{g}.\underline{b} = 1$, in the presence of $\underline{g}.\underline{b} = 2$ images. The effect is particularly dramatic when the loop is oriented so that its image major axis is almost parallel to $\underline{g}$. For example loops 1, 2 and 3 have the same Burgers vector a/3 $[11\bar{2}0]$ and, in Figure 6(f), $\underline{g}.\underline{b}$ is 1 for all three of them. However, loops 1 and 2 show strong contrast, whereas loop 3, which is differently oriented and has an image that is nearly parallel to $\underline{g}$, is in much weaker contrast.

As Maher & Eyre (1971) have shown, reversing the sign of $\underline{g}$ will, in most but not all cases, lead to a change of contrast of these weak images. Exceptions to this rule are exemplified by loops 4, 5 and 14 in Figures 6(f,g). When $\underline{g}$ is $\{20\bar{2}0\}$ and $\underline{g}.\underline{b}$ is either 0 or 2 (never 1), the loop contrast is much more uniform and anomalous weak images do not occur. Hence, these pseudo-invisible dislocation loop images can usually be recognised by reversing $\underline{g}$, by altering ω or the exposure conditions, or by changing to a different $\underline{g}$. The influence of ω on image strength of $\underline{g}.\underline{b} = 1$ loops will be considered in more detail in Section 3.4.

The results of the tilting and multiple-imaging experiment exemplified by Figure 6 establishes clearly that only a/3 $<11\bar{2}0>$ type Burgers vectors are present and that each of the three equivalent variants of this Burgers vector are equally represented. This latter conclusion is based on the observation that about one third of the loops go out of contrast in each micrograph taken with $\underline{g} = \{20\bar{2}0\}$. In a strict sense, the above analysis does not establish the magnitude of $\underline{b}$ and any Burgers vector of type a/n $<11\bar{2}0>$ would be consistent with the observations. Apart from the fact that a/3 $<11\bar{2}0>$ is by far the most likely type of a/n $<11\bar{2}0>$ Burgers vector in any hexagonal metal, the symmetric weak beam bright field (SWBBF) technique (Kelly & Blake 1973b) was used on occasions to establish the magnitude of $\underline{b}$ and prove that it was indeed a/3 $<11\bar{2}0>$. This technique can differentiate between dislocations with $\underline{g}.\underline{b} = 1$ and $\underline{g}.\underline{b} = 2$, since the latter gives very characteristic double images. When SWBBF images of irradiated zirconium were taken with $\underline{g} = \pm\{11\bar{2}0\}$, approximately one third of the loops showed double images ($\underline{g}.\underline{b} = 2$), whereas the remainder showed single images ($\underline{g}.\underline{b} = 1$) (see Figure 8). This is consistent with the Burgers vector being a/3 $<11\bar{2}0>$.

Finally, it is worth noting that the use of (0002) or (0004) reflections is not the only way to establish the presence or absence of pure $\underline{c}$ loops. Naturally this is the most obvious way, but it is prone to possible error in the presence of oxide or hydrides. The other approach is to compare loop densities in micrographs taken with $\{11\bar{2}0\}$ and $\{11\bar{2}2\}$. These two sets of micrographs will show the same number of $\underline{a}$ loops or ($\underline{c}$ + $\underline{a}$) loops, but any pure $\underline{c}$ loops will be absent in the $\{11\bar{2}0\}$ micrograph. Hence, if loop numbers are compared over the <u>same</u> area of foil (corrected for tilting if necessary), the pure $\underline{c}$ loops will appear as additional images in the $\{11\bar{2}2\}$ micrographs.

3.3 Loop Geometry

A rigorous and unequivocal characterisation of dislocation loops requires a knowledge of the loop plane normal position and the loop shape as well as the Burgers vector. This is particularly important in the case of non-edge loops; detailed descriptions of techniques for loop normal determinations have been given by Maher & Eyre (1971) and Kelly & Blake (1973a, 1974).

An inspection of the loops in Figures 6(a,g) reveals that in a foil orientation close to $[0\bar{1}10]$ the major axis dimension of the loop image exceeds the corresponding dimension in micrographs taken with the foil near the basal orientation [0001]. The obvious conclusion is that the loops in irradiated zirconium are not circular but elliptical, with the major axis of the loop approximately parallel to [0001]. Titanium shows analogous behaviour (Brimhall et al. 1971, Kelly & Blake 1974). The loop normal determination methods described by Maher & Eyre (1971) are based on the assumption that loops are circular and so cannot be used without modification for these elliptical loops in zirconium. Kelly & Blake (1974) have considered the case of elliptical loops and derived an analytical expression for determining the loop plane normal $\underline{n}$ and the ellipticity ratio b/a from measurements of true projected loop image minor (or major) axes in two accurately known orientations, related by a large tilt about an axis parallel to the major (or minor) axis of the loop, plus a knowledge of the trace of one of the elliptical loop semi-axes.

In the present work, this method was used on occasions. However, a variant of two surface trace analyses was found to be slightly simpler for elliptical loop normal determinations. As described in Appendix A, a two-surface trace analysis of elliptical loops in a thin foil cannot be carried out at any arbitrarily selected pair of foil orientations. This is because the images of elliptical loops do not always satisfy the condition that the long direction of the *image* is perpendicular to the normal to the loop plane. This violates the basic assumption inherent in two-surface trace analysis and leads to very considerable errors in the experimentally determined loop plane normal (see Appendix A — Figure A5). For elliptical loops with minor axis perpendicular to [0001] and major axis approximately parallel to [0001], the required conditions for two-surface trace analysis are satisfied at the prism and basal orientations. Hence, these two orientations are the only ones that can be used with confidence to determine elliptical loop plane normals in zirconium. A large-angle tilt stage and a suitable texture are necessary to reach these mutually perpendicular orientations.

The procedure adopted is as follows. In a prism orientation, the locus of all possible loop plane normal positions is plotted on a stereographic projection for each loop. This locus is the great circle containing the beam direction $\underline{z}$ and the normal to the loop *image* major axis. The foil is then tilted from prism to basal orientation and micrographs are taken at 10 or 15° intervals during the tilting operation to keep track of each individual loop. These intermediate micrographs are particularly important as some of the loops may go into weak contrast and effectively disappear, only to reappear later in the tilting sequence. This is invariably associated with the pseudo-invisible $\underline{g}.\underline{b} = 1$ images referred to previously; it can often be avoided by taking the opposite $\underline{g}$ micrograph in each case. At the basal orientation, the trace analysis is repeated giving a second locus of possible loop plane normals. These two loci intersect at approximately 90° and the point of intersection defines the loop plane normal to within ± 5° or better (see Appendix A — Figures A3, A4).

Note that care is necessary when performing the trace analysis at the prism orientation. If the loop in question is almost perpendicular to the beam, the trace error can be considerable. In Figure A4, this corresponds to a loop with normal $\underline{n}$ in a foil with $\underline{z}$ parallel to $[10\bar{1}0]$. For loops that are more nearly edge-on (i.e. loop with normal $\underline{n}$ in a foil with $\underline{z}$ near $[1\bar{1}00]$ or $[1\bar{2}10]$ — Figure A4), the trace errors are much less and these edge-on loops can be used to establish that the angle between the loop major axis $\underline{a}$ and the direction [0001] is invariably less than 20°. Whenever trace analysis was performed at a prism orientation, the predominantly edge-on loops were analysed and the ones almost normal to the beam were avoided wherever possible.

The results of loop normal determinations for a number of the loops shown in Figure 6 are plotted in a single triangle of the stereographic projection in Figure 9. These results are similar to those already reported for post-irradiation annealed zirconium. There is no evidence that loop character (i.e. vacancy or interstitial) or loop ellipticity has any significant effect on the loop normal position. The loop normals exhibit a marked departure from the pure edge configuration, being tilted towards one of the neighbouring $\{10\bar{1}0\}$ poles and, to a lesser extent, towards (0001). This behaviour is well illustrated by loops 1, 2 and 3 in Figure 6. These three loops have the same Burgers vector $\underline{b} = a/3\ [11\bar{2}0]$, yet the trace analysis shows that loops 1 and 2 have normals close to $[10\bar{1}0]$, whereas loop 3 has a normal which is rotated half way towards $[0\bar{1}10]$. The additional rotation of the loop normal towards [0001] is best seen in the case of loops that are almost edge-on in a prism orientation. Thus, loop 8 in Figure 6(a) is tilted slightly more towards [0001] than loop 7.

The loop ellipticity was determined from averages of the loop image major axis measurements from ± $\underline{g}$ images in two orientations — one close to a prism direction, such as $[0\bar{1}10]$, and the other close to [0001]. This gives 2a and 2b, the loop major and minor axes respectively. The small loop tilt component towards [0001] does mean that the magnitude of 2a is slightly underestimated but, since this varies as the secant of the tilt, the magnitude of the error is in general less than the accuracy of the measurements (see Appendix A).

The way in which such results are presented is worth considering. Measurements must be made at both prism and basal orientations to establish the loop ellipticity, and this allows the choice of plotting the data as b/a vs 2a or b/a vs 2b as shown in Figure 10. Note the pronounced cut-off at about 200 nm corresponding to the limit in loop size imposed by the foil thickness, i.e. loops with 2a greater than the foil thickness do not appear as complete loops on the micrographs used to determine the loop ellipticity. Although the b/a vs 2a plots are readily understood, the alternative plot of b/a vs 2b (Figure 10(b)) is more confusing. The tendency of the data points to congregate in a small range of 2b at low b/a values is a consequence of the loop size/foil thickness limit. The b/a vs 2a plot is therefore to be preferred as a more accurate indication of the dependence of ellipticity on loop size.

The results of ellipticity measurements in loops irradiated over a range of conditions are summarised in Figure 11. Within the wide scatter, the results are similar to those previously obtained on post-irradiation annealed titanium (Kelly & Blake 1974), except that the present results extend over a larger range of loop sizes. More important, the interstitial loops appear to behave in a different manner from the vacancy loops. The variations of b/a with loop size were determined by averaging the results in Figure 11 over convenient size intervals and the trends are shown in Figure 12. The interstitial loops are almost circular (with $b/a \simeq 0.94$) independent of loop size, whereas vacancy loops are essentially elliptical with b/a ratios decreasing from about 0.8 in the range of 2a of 0-40 nm to 0.6 for loops with 2a in excess of 100 nm.

3.4 Loop Nature

The classification of dislocation loops into vacancy and interstitial components is one of the most important steps in the complete description of the defect structure in irradiated metals. In the previous sections it has been clearly established that all the loops in c.p.h. zirconium irradiated at 400°C have $a/3\langle 11\bar{2}0\rangle$ Burgers vectors and that the loops are tilted from the pure edge orientation. Consequently, the determination of the vacancy and interstitial character of the loops can be made in terms of the rules given by Kelly & Blake (1973a) in their study of dislocation loops in post-irradiation annealed zirconium.

Essentially their method follows the procedure originally suggested by Maher & Eyre (1971) and involves getting the specimen in a position where at least the majority of the loops are in a 'safe' orientation. A safe orientation can be defined as one where $\underline{g}.\underline{b}$ and $\underline{b}.\underline{z}$ have the same sign when $\underline{g}.\underline{n}$ is positive or $\underline{g}.\underline{b}$ and $\underline{b}.\underline{z}$ have opposite signs when $\underline{g}.\underline{n}$ is negative. In a safe orientation, an interstitial loop will behave in the established fashion and appear in outside contrast when both $\underline{g}.\underline{b}$ and ω are positive. A vacancy loop will show the opposite behaviour and will be in outside contrast when $\underline{g}.\underline{b}$ is negative (ω still positive). For zirconium, micrographs taken in $\underline{g} = \pm\{11\bar{2}2\}$ near one of the $\langle 11\bar{2}3\rangle$ orientations* will have two thirds of the loops in a safe orientation. This assumes that the loop habit planes are as shown in Figure 9. If the location of the [0001] direction is known relative to the foil orientation, these safe loops can be analysed with reference to Figure 13, which shows that interstitial loops are in outside contrast when $\underline{g}$ points towards [0001] (ω positive).

The application of the method and the precautions required to achieve an unambiguous loop identification will be illustrated with examples based on the loops shown previously in Figure 6. Thus, Figure 14 shows these loops imaged in an orientation close to $[1\bar{2}13]$ with $\underline{g} = \pm(1\bar{2}1\bar{2})$ and ω positive. Loops with $\underline{b} = \pm\, a/3\, [\bar{1}2\bar{1}0]$, i.e. 4, 5, 13 and 14, are in a safe orientation and $\underline{g}.\underline{b} = \pm 2$. A characteristic of $\underline{g}.\underline{b} = 2$ loops is their strong contrast and large shifts in loop image width with change in the sign of $\underline{g}$. Loops with $\pm\, a/3\, [11\bar{2}0]$ and $\pm\, a/3\, [\bar{2}110]$ Burgers vector give $\underline{g}.\underline{b} = \pm 1$. If the loop normals are tilted towards $[0\bar{1}10]$ and $[1\bar{1}00]$ respectively, these $\underline{g}.\underline{b} = 1$ loops are in a 'safe' orientation (Kelly & Blake 1973a). This 'safe' orientation can be recognised from the direction of the loop trace relative to $\underline{g}$. Loops with a trace inclined by more than 30° are 'safe', but those

---

* Note that the $\langle 11\bar{2}3\rangle$ orientation in the paper by Kelly & Blake (1973) is labelled incorrectly as $\langle 11\bar{2}4\rangle$.

inclined at less than 30° to $\underline{g}$ are in an 'unsafe' orientation. For example, loops 1, 2, 6, 7, 8, 11 and 12 are in an unsafe orientation. Other $\underline{g}.\underline{b} = 1$ loops such as 3, 9, 10 and 15 are in a 'safe' orientation but the image shifts with $\pm\ \underline{g} = (1\bar{2}1\bar{2})$ are much smaller than for $\underline{g}.\underline{b} = 2$ loops.

Loops 'unsafe' in the $\underline{z} = [1\bar{2}13]$ foil orientation can be rendered 'safe' by tilting the foil to another $\langle 1\bar{2}13\rangle$ orientation, e.g. $\underline{z} = [2\bar{1}\bar{1}3]$, and imaging the loops with $\underline{g} = \pm\ (\bar{2}112)$, as shown in Figure 15. By using two $\langle 11\bar{2}3\rangle$ orientations, all the loops in a given field can be characterised.

Unfortunately, some of the loops imaged in Figure 14 display the features associated with $\underline{g}.\underline{b} = 1$ images referred to previously. Depending on the magnitude of ω, $\underline{g}.\underline{b} = \pm\ 1$ loops with traces nearly parallel to $\underline{g} = \pm\ (1\bar{2}1\bar{2})$ are often in weak contrast, e.g. loops 1, 2 and 11 in Figure 14(c) and loop 12 in Figure 14(a). The behaviour of loop 12 in Figures 14(a,b) is typical of the observations of Maher & Eyre (1971) on tilted edge loops in molybdenum; they showed that pseudo-invisibility is obtained when 'there are combinations of $\underline{z}$, $\underline{b}$, $\underline{n}$, $\underline{g}$, $\underline{s}$ and loop depth resulting in $\underline{g}.\underline{b} \neq 0$ images in terms of either topography or strength of contrast which are similar to those expected when $\underline{g}.\underline{b} = 0$'. These weak or pseudo-invisible $\underline{g}.\underline{b} = 1$ loops can make loop characterisation more difficult, even when two $\langle 11\bar{2}3\rangle$ orientations are used.

To achieve a completely unambiguous loop characterisation, it would therefore be preferable to restrict the analysis to loops with $\underline{g}.\underline{b} = 2$. This means that for the best possible results, particularly when the loops are smaller than in the present example, three $\langle 11\bar{2}3\rangle$ foil orientations are required so that appropriate $\underline{g}$ values can be selected to give one $\underline{g}.\underline{b} = 2$ case for each loop in the field.

The characterisation of dislocation loops in zirconium has been described specifically in terms of $\langle 11\bar{2}3\rangle$ foil orientations. Admittedly, this is particularly convenient for thin foils made from sheet or tubing, where the texture of such material allows the $\langle 11\bar{2}3\rangle$ orientation to be reached with only a small amount of specimen tilt. However, this is not the only situation where the loops are in a safe orientation, and other foil orientations and operating reflections can be used. Such alternatives may be necessary in specimens with a less amenable texture; for example, discs cut at right angles to a bar or rod with a strong axial prism texture. The other point that should be emphasised is that loop characterisation can be carried out even when none of the loops are in a safe orientation. Unfortunately, the procedure in this case is extremely tedious since the habit plane, or at least the approximate position of $\underline{n}$, must be established for each individual loop before it is characterised.

3.5 Quantitative Results

The quantitative description of the loop structure in irradiated materials requires the determination of the loop size spectrum and the concentration of both vacancy and interstitial components of the damage. For circular loops, this procedure is relatively straight-forward since the loop size is uniquely defined by the loop diameter; this is always given directly from measurements of the loop image major axis in any foil orientation. However, with elliptical loops two parameters, the major (2a) and minor axes (2b), are necessary to describe the size accurately.

Naturally, measuring both 2a and 2b, and at the same time determining the loop character, involves considerable labour, so there is a temptation to restrict the measurements to one size parameter, i.e. either 2a or 2b. However, the normal texture of zirconium alloy tubing or sheet is such that the basal orientation is generally more accessible than the prism orientation, even with good electron microscope specimen tilting stages. This means that 2b measurements are the easiest to obtain. Relying on 2b measurements alone could lead to misleading and erroneous results, so a practical compromise for loop distribution measurements is required.

A series of loops measured on an area of the micrograph which included the loops discussed in the b/a plots of Figure 10 yielded the size distribution shown in Figure 16. It is immediately obvious that, for an identical loop population, the vacancy loop distribution is broader in the 2a plot than in the 2b plot. Furthermore, the peak of the distribution is about 120 nm in the 2a plot whereas it is near 70 nm for the 2b plot. On the other hand, the interstitial loop distribution is not altered significantly by the method of presentation of the results. Obviously, if the ellipticity of the loops is neglected, the size distributions will be markedly influenced by the foil orientation at which quantitative measurements are made, i.e. is 2a, 2b or some intermediate diameter being measured?

The need to consider ellipticity is even more acute when it is necessary to derive the number of interstitial and vacancy defects present in the loops. The number of interstitials or vacancies clustered in a loop is proportional to the loop area which, for elliptical loops, is given by πab and for circular loops by πr^2, where r is the radius of a circular loop. Table 1 compares the vacancy and interstitial contents in the loop population recorded in Figure 16(a,b).

In Table 1 no correction has been made for the non-edge character of the loops. This correction factor is given by $\cos\psi$, where ψ is the angle between $\underline{n}$ and $\underline{b}$. For the loops analysed here ψ is about 20-30° and there is no indication that vacancy and interstitial loops have different average values of ψ. As the correction factor is close to unity, and applies equally to circular and elliptical loops, it has not been included in the data in Table 1. If other zirconium alloys turn out to have ψ values > 30°, or show a marked difference in ψ between the two types of loop, it might be necessary to include this correction factor in the estimates of point defect numbers.

From measurement of 2a and 2b on each loop in the population, the interstitial content in the loops is estimated to be 28 per cent. On the other hand, if the measurements were made either near the basal or prism orientation and the loops were assumed to be circular, the interstitial content would have been estimated as 37 and 20 per cent respectively. A more striking discrepancy would have occurred if the number of defects in vacancy loops was estimated from prism and basal orientations, in which case the results would have differed by a factor of 2.5. Table 1 also reveals that the true vacancy and interstitial content could have been estimated satisfactorily from either 2a or 2b measurements if b/a values of 0.94 and 0.6 respectively were assumed for interstitials and vacancies, regardless of size.

TABLE 1

COMPARISON OF VACANCY AND INTERSTITIAL LOOP AREAS

Equation for Loop Area	Total Loop Area (nm^2)			Interstitial Content (%)
	Interstitials	Vacancies	Undetermined	
$\pi/4\ \Sigma(2a)(2b)$	3830	9890	31	28
$\pi/4\ \Sigma(2a)^2$	3970	15900	36	20
$\pi/4\ \Sigma(2b)^2$	3640	6280	27	37
$0.6\ \pi/4\ \Sigma(2a)^2$	—	9540	22	28
$0.94\ \pi/4\ \Sigma(2a)^2$	3730	—	34	
$\frac{\pi}{0.6 \times 4}\ \Sigma(2b)^2$	—	10460	45	27
$\frac{\pi}{0.94 \times 4}\ \Sigma(2b)^2$	3870	—	28	

Eyre et al. (1971) consider that the loop size spectrum should include loops which cannot be identified unambiguously as well as those that can be classified into vacancy and interstitial groups. In the example used in Figure 16 and Table 1, these unidentified loops represent an insignificant fraction of the total defect population. Failure to obtain an unambiguous result arose for two reasons; either the loops were too small for the inside/outside image shifts to be revealed clearly, or overlap of images occurred so that it was not possible to follow a given loop through all of the tilting operations.

Similar measurements within other grains of the same thin foil revealed significant variations in the I/V loop ratio (Figure 17). In other respects, the size distributions were reasonably similar, as shown by the peaking of the vacancy loop population near 70 nm in the 2b plots of Figure 16(a) and Figure 17. Since the foil used in the latter example was thicker, the vacancy loop spectrum extends to larger values of 2b (or 2a). Such grain to grain variations in the relative loop population were frequently encountered despite the large number of loops sampled in each determination. It must, therefore, be accepted that these grain to grain variations in the interstitial to vacancy loop ratio are real and that it is not possible to assign a particular value for a specific irradiation temperature and fluence in a given material without including large scatter bands.

Finally, it is clear that the type of measurements necessary for the rigorous loop distribution and characterisation discussed in this section are impractical in cases where the loop size range is very small and/or the defect density is high. Under these conditions, it would be impossible to carry out the loop identification at a $\langle 11\bar{2}3\rangle$ orientation and then maintain the identity of each loop while the foil is tilted to both the prism and basal orientations needed to obtain accurate measurements of 2a and 2b respectively. For such loop populations, it would be better to carry out loop identification and size measurements at $\langle 11\bar{2}3\rangle$ orientations and then ignore loop ellipticity completely. The errors of such a procedure will not be excessive, since even the vacancy loops tend to become more circular below 40 nm, and the errors in loop size measurement at $\langle 11\bar{2}3\rangle$ are such that the loop image major axis corresponds to some intermediate size between 2a and 2b for most loops.

4. CONCLUSIONS

The analysis of radiation-induced dislocation loops in zirconium and its alloys requires particular care. In addition to the normal procedures adopted in transmission electron microscopy, the following points must always be kept in mind.

(a) Beware of confusing small hydrides and surface oxide particles with true defect cluster images. Large hydrides are easily recognised by their characteristic images, whereas the rare case of small hydrides may require stereo pairs or careful black/white contrast analysis to distinguish their images from small damage clusters. This is particularly important in (0002) micrographs. To avoid the confusing effect of the surface oxide background contrast take micrographs with relatively large ω (> 1.0). When attempting to identify $\underline{c}$ component loops use the (0004) in preference to the (0002) reflection.

(b) Double images will be produced if $\{10\bar{1}0\}$ is set up so that $\{20\bar{2}0\}$ is also diffracting strongly with a negative ω. Always use $\{20\bar{2}0\}$ with a positive ω in preference to $\{10\bar{1}0\}$.

(c) When taking micrographs for Burgers vector identification, always work in *flat* areas of the foil to ensure that strict two-beam conditions are obeyed. Be very careful to avoid stray reflections particularly in the critical case of $\underline{g}$ = (0002) or (0004). Remember that the presence of the forbidden (0001) spot in a (0002) or (0004) micrograph is an absolute guarantee that two-beam conditions are *NOT* obeyed. Unfortunately, the reverse is not true and the absence of the forbidden (0001) cannot be taken to mean that conditions are favourable. In general, any micrograph in which two-beam conditions do *not* apply is useless for Burgers vector identification via the $\underline{g}.\underline{b} = 0$ criterion.

(d) Always check suspected $\underline{g}.\underline{b} = 0$ images to ensure that they are true residual images and not the anomalous weak $\underline{g}.\underline{b} = 1$ images. These weak images occur with $\{11\bar{2}0\}$ or $\{11\bar{2}2\}$, particularly when $\underline{g}$ is approximately parallel to the loop image major axis. Reversing the sign of $\underline{g}$, altering ω or changing to a different $\underline{g}$ will usually differentiate this pseudo-invisibility from a true $\underline{g}.\underline{b} = 0$ condition.

(e) For reliable loop plane normal determinations and loop size measurements it is essential to obtain micrographs of the same area at both the prism and the basal orientations. Admittedly, this is difficult to do in practice and, in some cases, may be beyond the capacity of the microscope tilt stage. However, for each series of specimens examined, it is worth attempting this in at least one area — if only to ensure that the loop plane normals and ellipticities follow the pattern established in previous work.

(f) Make absolutely certain that the foil is in a 'safe' orientation before attempting to establish the character of any dislocation loop. This requires a knowledge of the loop plane normal, based on experiment or faith, plus a recognition that a given orientation is not invariably 'safe' for all the loops in the field. For example, experience indicates that <11$\bar{2}$3> is a 'safe' orientation, but only for two thirds of the a/3 <11$\bar{2}$0> loops in the field. As a result, to characterise all the loops in the field, TWO series of micrographs must be taken using different <11$\bar{2}$3> orientations. If possible, use three <11$\bar{2}$3> orientations chosen so that every loop in the area satisfies the condition $\underline{g}.\underline{b} = 2$ in one of these three sets of micrographs, and then analyse only the $\underline{g}.\underline{b} = 2$ loops in each particular orientation.

(g) If accurate estimates are required of loop size distributions or point defect concentrations in the loops, the ellipticity must be taken into account. This means that both the major and minor axes of each loop should be measured, although small loops (< 30 or 40 nm in size) can probably be assumed to be circular without introducing uncertainties greater than the measurement errors. Alternatively, it can be assumed that the work described here on pure zirconium irradiated at 668 K (395°C) applies to ANY irradiated zirconium alloy, i.e. interstitial loops are always circular while vacancy loops above 30 nm in size have an average ellipticity of 0.6. This is certainly the easy way out, but it would be more satisfactory if this situation could be shown experimentally to apply to other zirconium alloys over a range of irradiation conditions.

5. ACKNOWLEDGEMENTS

The authors gratefully acknowledge Dr. C.J. Ball for his critical review of the manuscript.

6. REFERENCES

Adamson, R.B., Bell, W.L. & Lee, D. (1974) - Zirconium in Nuclear Applications. ASTM-STP 551, p.215

Bedford, A.J. & Miller, D.R. (1972)-J. Aust. Inst. Met.,17: 120

Bell, W.L. (1975)-J. Nucl. Mater., 55: 14

Blake, R.G., Kelly, P.M. & Warren, R.B. (1972) - Proc. 5th European Congress on Electron Microscopy, Manchester, Inst. of Physics, p.340

Blake, R.G., Jostsons, A. & Kelly, P.M. (1974) - 8th Int. Congress on Electron Microscopy, Canberra, Aust. Acad. of Science, Vol. 1, p.610

Brimhall, J.L., Kulcinski, G.L., Kissinger, H.E. & Mastel, B., (1971) - Radiat. Eff., 9: 273

Carpenter, G.J.C. (1973)-J. Nucl. Mater., 48: 264

Eyre, B.L., Maher, D.M. & Bartlett, A.F. (1971) - Philos. Mag.,23: 439

Fisher, E.S. & Alfred, L.C.R. (1968) - Trans. Met. Soc. AIME.,242: 1275

Gelles, D.S. & Harbottle, J.E. (1974) - CEGB Report RD/B/N2973

Gilbert, R.W. (1975) - Proc. 2nd Ann. Gen. Meeting, Microscopical Society of Canada

Gulden, T.D. & Bernstein, I.M. (1966) - Philos. Mag.,14: 1087

Hastings, I.J., Howe, L.M. & Ploc, R.A. (1974) - AECL Report 4363

Head, A.K., Humble, P., Clarebrough, L.M., Morton, A.J. & Forwood C.T. (1973) - Computed Electron Micrographs and Defect Identification. North Holland, Amsterdam

Hirsch, P.B., Howie, A., Nicholson, R.B., Pashley, D.W. & Whelan, M.J. (1965) - Electron Microscopy of Thin Crystals. Butterworths, London

Kelly, P.M. & Blake, R.G. (1973a) - Philos. Mag.,28: 415

Kelly, P.M. & Blake, R.G. (1973b) - Philos. Mag.,28: 475

Kelly, P.M. & Blake, R.G. (1974) - Phys. Status Solidi A,25: 599

Kelly, P.M., Blake, R.G. & Jostsons, A. (1975) submitted to J. Nucl. Mater.

Lee, D. & Koch, E.F. (1974) - J. Nucl. Mater.,50: 162

Madden, P.K. (1974) - CEGB Report RD/B/M3125

Maher, D.M. & Eyre, B.L. (1971) - Philos. Mag., 23: 409

Northwood, D.O. (1975) Proc. 2nd Ann. Gen. Meeting, Microscopical Society of Canada

Northwood, D.O. & Gilbert, R.W. (1973) - J. Aust. Inst. Met., 18: 158

Northwood, D.O. & Gilbert, R.W. (1974) - J. Nucl. Mater., 51: 271

Okamoto, P.R., Levine, E. & Thomas, G. (1967) - J. Appl. Phys., 38: 289

Okamoto, P.R. & Thomas, G. (1968) - Phys. Status. Solidi,25: 81

Partridge, P.G. (1967) - Met. Reviews,118: 169

Riley, A. & Grundy, P.J., (1972) - Phys. Status Solidi A,14: 239

Rühle, M. (1969) Proc. Symp. on Radiation Damage in Reactor Materials Vol. 1, IAEA, Vienna, 26 June, p.113

Rühle, M. (1971) - Radiation Induced Voids in Metals, Proc. Int. Conference, Albany, N.Y. 9-11 June (eds. Corbett, J.W. & Ianiello, L.C.) USAEC CONF-710601, p.255

FIGURES 1 TO 17

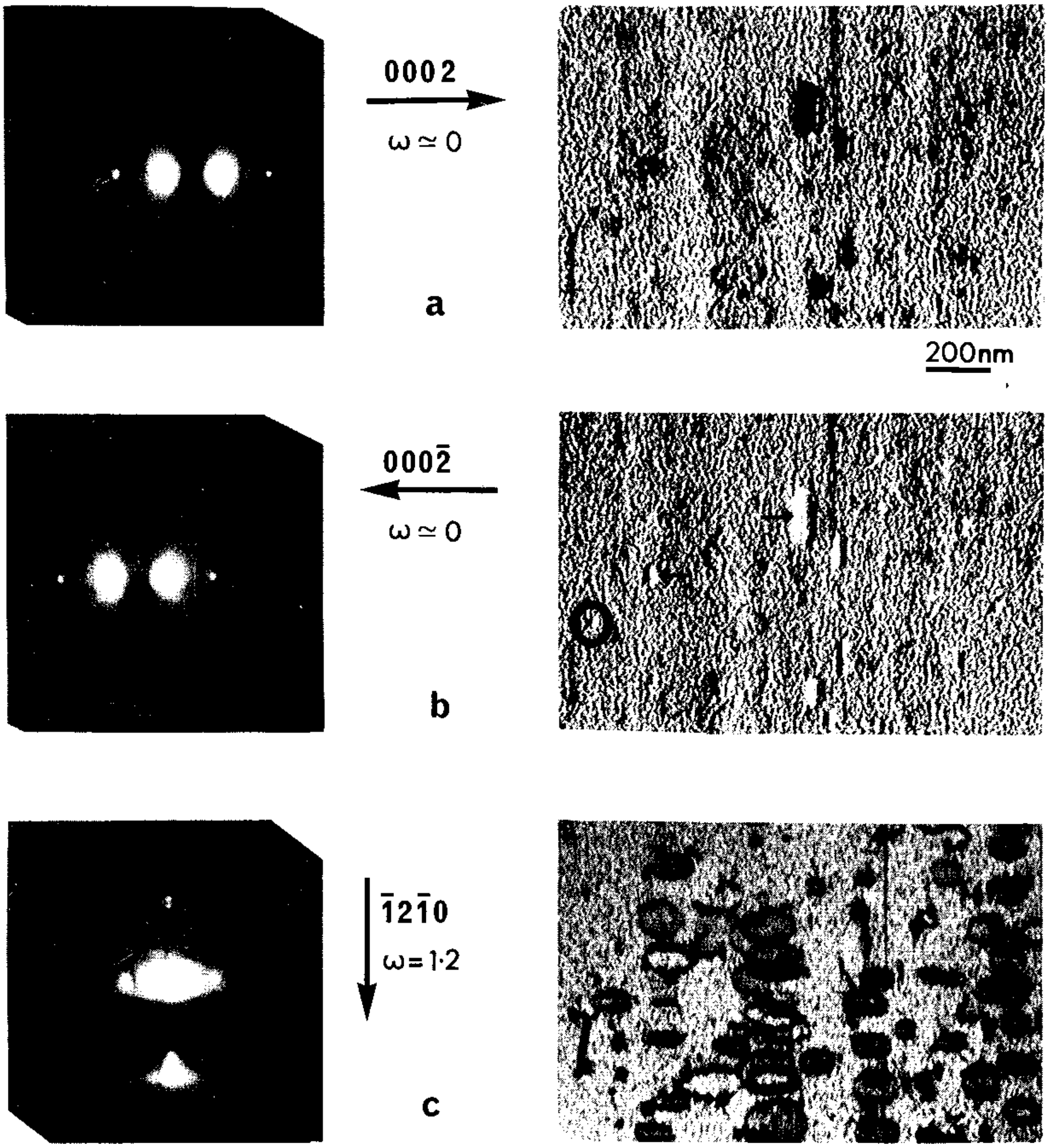
0002
ω ≃ 0
a
200nm
000$\bar{2}$
ω ≃ 0
b
$\bar{1}2\bar{1}0$
ω = 1·2
c

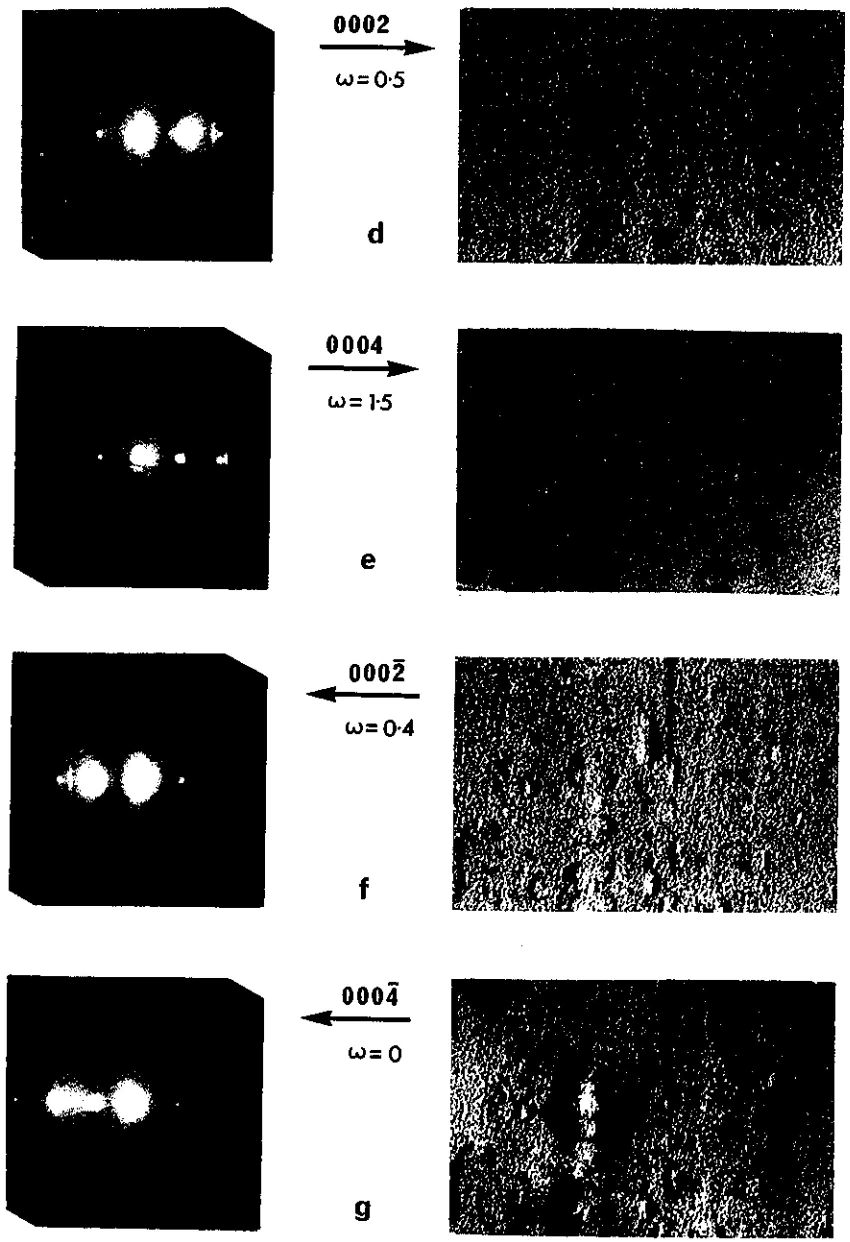

FIGURE 1 EFFECT OF ω ON OXIDE AND HYDRIDE CONTRAST IN ZONE REFINED ZIRCONIUM IRRADIATED AT 668 K (395°C) TO 6.4×10^{23} neutrons m^{-2} (> 1 MeV)

In all cases the foil is oriented so that the electron beam ($-\underline{z}$) is approximately parallel to $[10\bar{1}0]$.

In (a) and (b) the surface hydrides are showing anomalous strain contrast images with a black 'tail' in (a) and a white tail in (b). Note that in (b) the arrowed hydrides show white tails pointing in opposite directions, indicating that these two hydrides are on opposite surfaces of the foil. The encircled hydride in (b) is less than 20 nm in size.

In (c) $\underline{g}$ is $(\bar{1}2\bar{1}0)$ and dislocation loops, which were previously out of contrast in (a) and (b), now show strong images, whereas the hydride images are faint.

Figures (d) and (f) demonstrate the decrease in oxide contrast achieved by increasing ω for the (0002) reflection from zero to about 0.5. Further decrease in the oxide contrast occurs with $\underline{g} = (0004)$ — Figures (e) and (g). In particular note that the hydride contrast remains strong and the characteristic residual $\underline{g}.\underline{b} \times \underline{u}$ contrast from the $a/3\langle 11\bar{2}0\rangle$ dislocation loops is clearly visible in (e) and (g). All micrographs taken at 200 kV.

FIGURE 2 COMPARISON OF OXIDE CONTRAST WITH SMALL LOOP CONTRAST

Figures (a) and (b) are from unirradiated crystal bar zirconium taken with g = ±(0002) showing pronounced oxide film contrast. The oxide particle arrowed in (a) resembles the image of a dislocation loop about 15 nm in diameter. In the opposite g micrograph (b) the arrowed particle reverses contrast. Figures (c) and (d) show true dislocation loop images in crystal bar zirconium irradiated to 2 x 10^{23} neutrons m^{-2} at 573 K (300°C). In this pair of micrographs g is ±($11\bar{2}0$) and the arrowed dislocation loop images do NOT reverse contrast, but show the typical inside/outside behaviour. All micrographs taken at 100 kV.

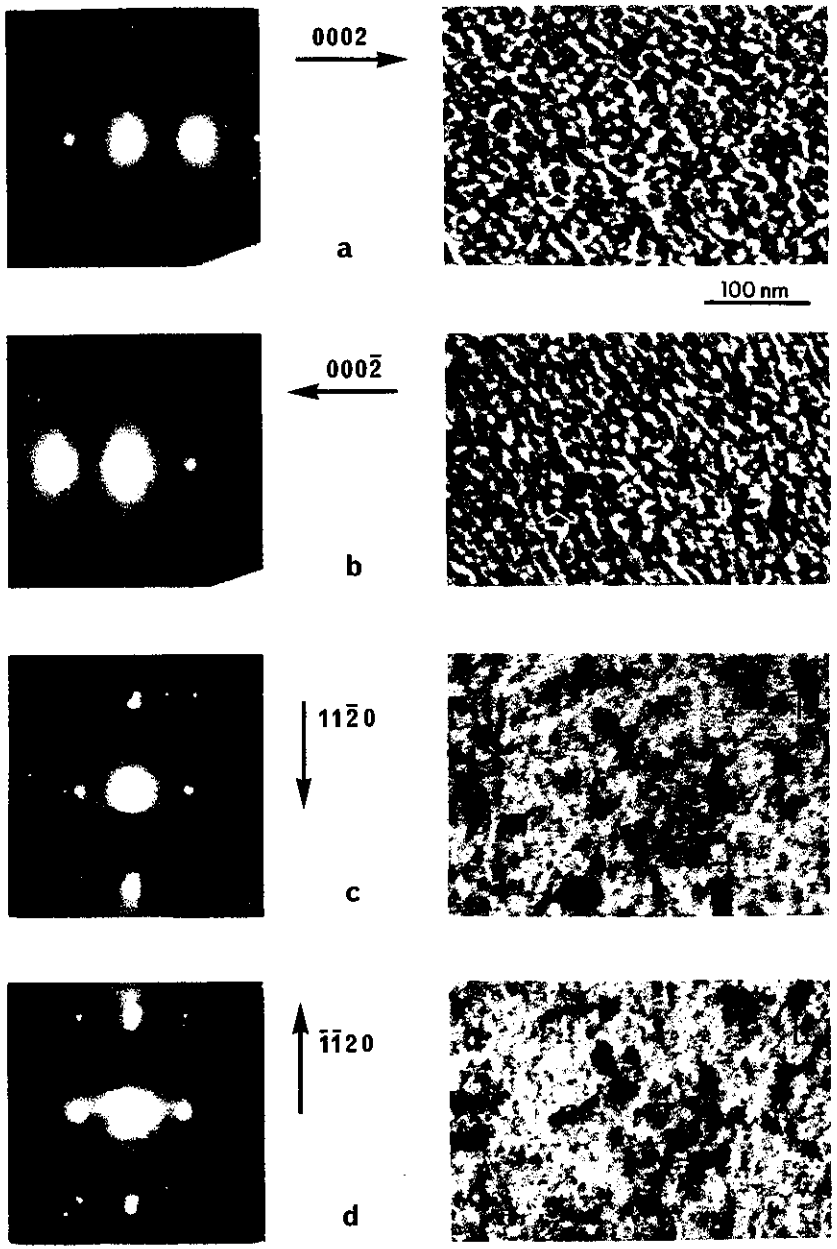

FIGURE 3 DARK FIELD IMAGE OF OXIDE REFLECTION (CIRCLED BY APERTURE) SHOWING SURFACE OXIDE PARTICLES OF APPROXIMATELY 10 nm DIAMETER ($\underline{z} \approx [10\bar{1}0]$; 200 kV).

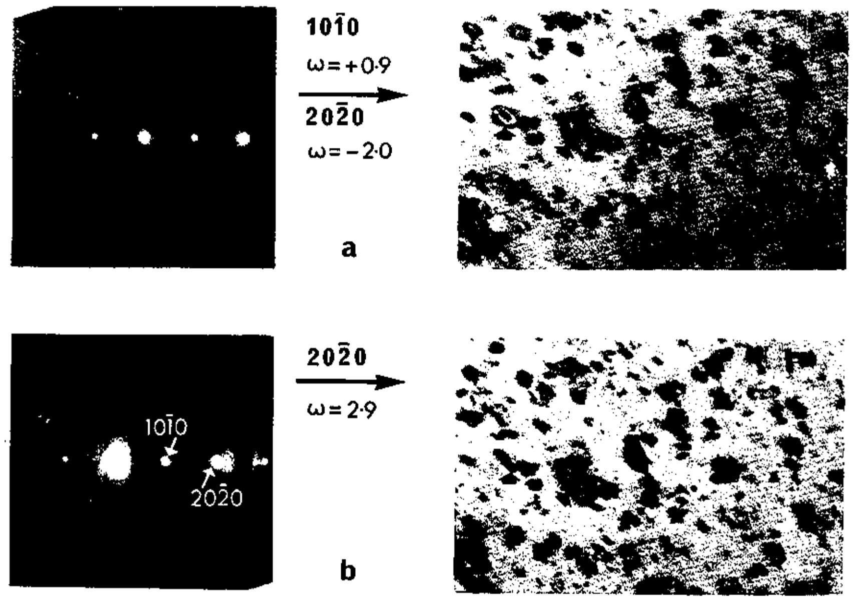

FIGURE 4 LOOP IMAGE DOUBLING WITH $(10\bar{1}0)/(20\bar{2}0)$ REFLECTIONS.

In (a) the arrowed loops show double images resulting from the combination of a small negative ω for $(20\bar{2}0)$ and a positive ω for $(10\bar{1}0)$. Note the almost complete absence of the $(10\bar{1}0)$ Kikuchi line. The double loop images become conventional single images when $g = (20\bar{2}0)$ is excited with a positive ω (Figure (b); 100 kV).

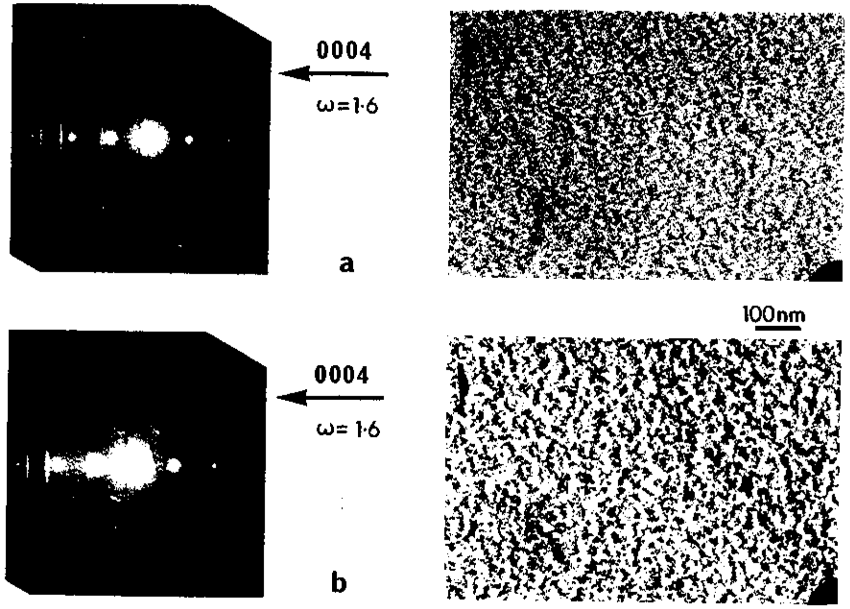

FIGURE 5 EFFECT OF ELECTRON BEAM EXPOSURE ON THE OXIDE CONTRAST IN UNIRRADIATED ZIRCONIUM

Figure (b) was recorded after 40 minutes in the electron beam, whereas (a) was taken at the beginning of the examination. Despite the identical imaging conditions, the oxide contrast has been significantly increased by the exposure to the beam (200 kV).

FIGURE 6 BURGERS VECTOR ANALYSIS IN ZONE REFINED ZIRCONIUM IRRADIATED AT 668 K (395°C) TO 6.4 x 10^{23} neutrons m^{-2} (> 1 MeV).

Loop alignment in bands parallel to the (0001) plane is shown in (a), (b) and (d). The absence of loop contrast in $\underline{g}$ = (0002), Figure (c), demonstrates clearly that the loop Burgers vectors do <u>not</u> possess a $\underline{c}$ component. Loops arrowed in (d) show typical residual contrast characteristic of $\underline{g}.\underline{b} = 0$ and $\underline{g}.\underline{b} \times \underline{u} \neq 0$.

On tilting from the prism orientation towards the basal orientation, the loop alignment on (0001) becomes less obvious - (e) and (f). The loop image major axes at (0001) are significantly smaller than those imaged near the prism orientations, indicating that the loops are predominantly elliptical with the major axis approximately parallel to [0001] and the minor axis within the basal plane.

Figure (h) to (j) imaged in various {20$\bar{2}$0} reflections near [0001] permit the assignment of specific a/3<11$\bar{2}$0> Burgers vectors to the loops.

Figure (k) is a Kikuchi map indicating the orientations at which the various images were recorded for Figures 6, 14 and 15. In general, a tilt of about 4° from the nearest indexed Kikuchi pole was required to set up strict two-beam reflection conditions. (200 kV).

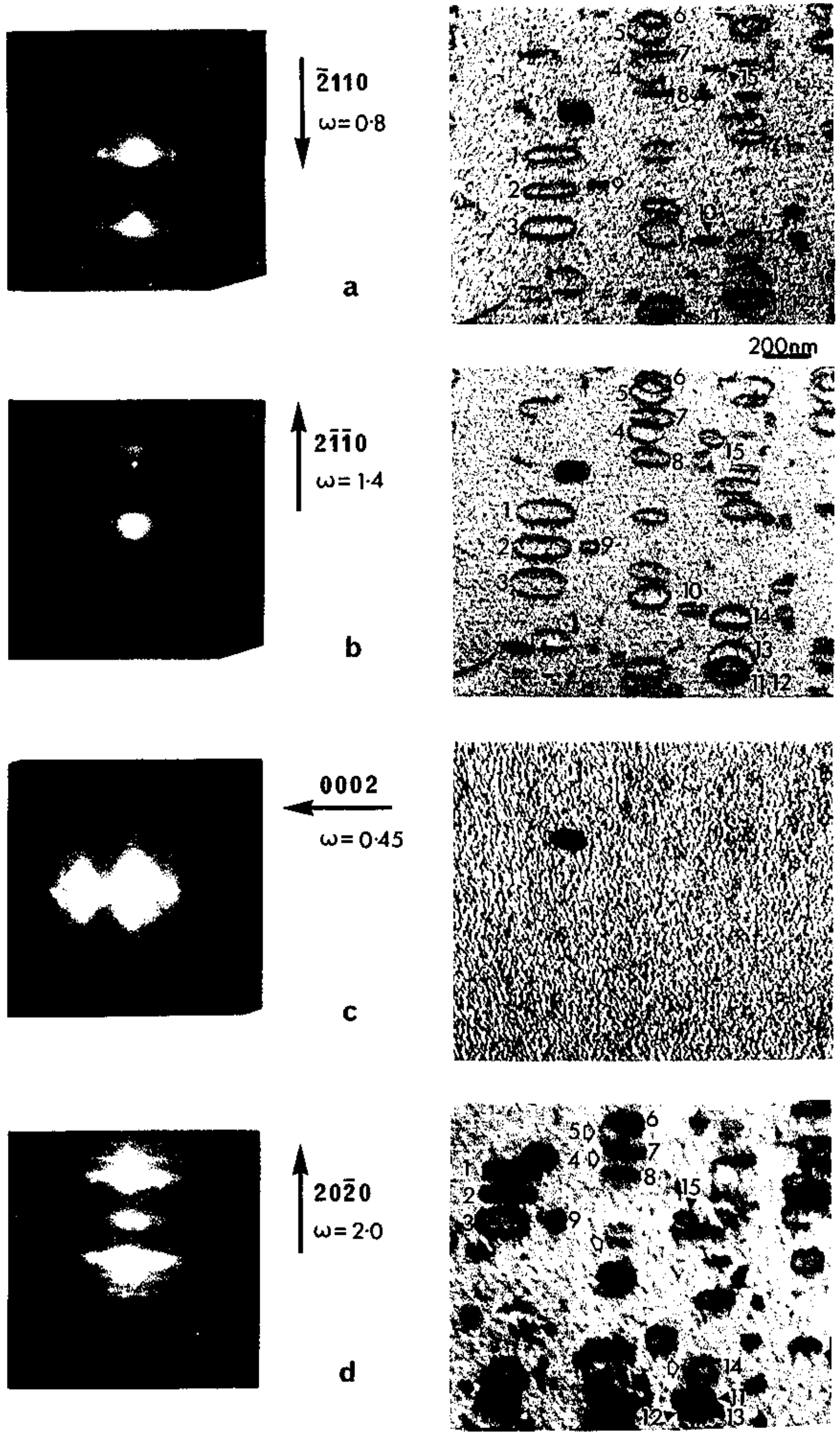

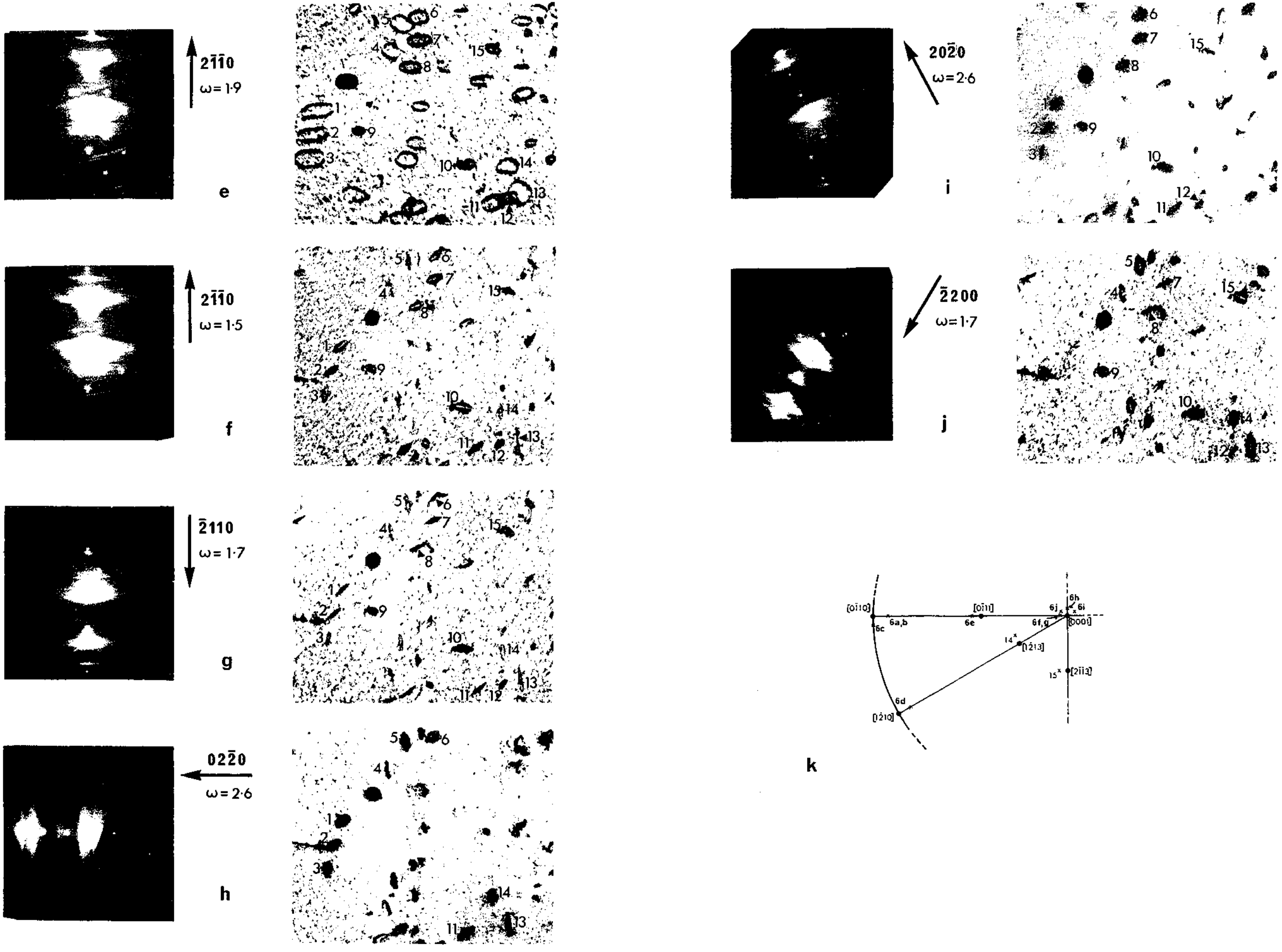
$2\bar{1}\bar{1}0$
ω = 1·9
e
$2\bar{1}\bar{1}0$
ω = 1·5
f
$\bar{2}110$
ω = 1·7
g
$02\bar{2}0$
ω = 2·6
h
$20\bar{2}0$
ω = 2·6
i
$\bar{2}200$
ω = 1·7
j
1
2
3
4
5
6
7
8
9
10
11
12
13
14
15
$[0\bar{1}10]$
$[0\bar{1}11]$
$[0001]$
$[1\bar{2}13]$
$[2\bar{1}\bar{1}3]$
$[1\bar{2}10]$
6a,b
6c
6d
6e
6f,g
6h
6i
6j
14
15
k

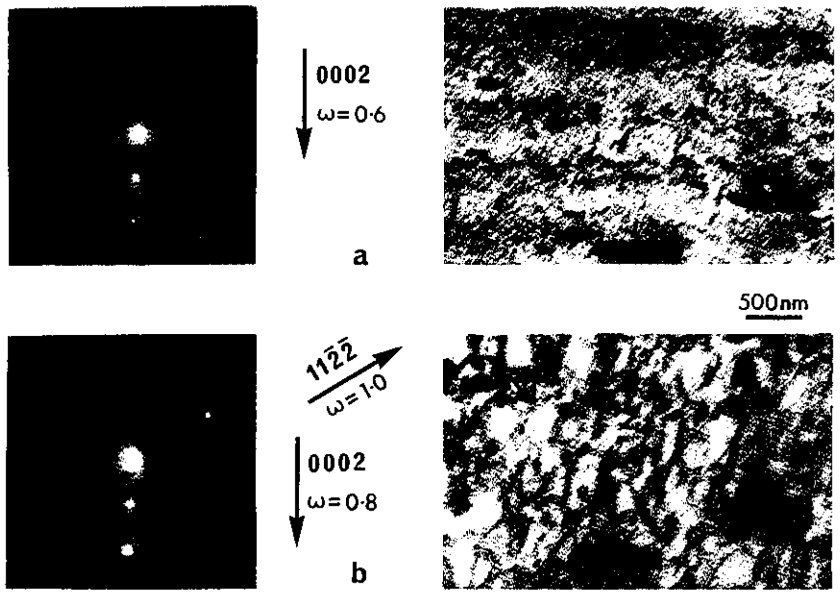

FIGURE 7   ZONE REFINED ZIRCONIUM IRRADIATED AT 668 K (395°C) TO 1.8×10^{24} neutrons m^{-2} (> 1 MeV) SHOWING THE EFFECT OF NOT ADHERING TO STRICT TWO-BEAM CONDITIONS.

In (a) only (0002) is operating and the loops exhibit the residual contrast expected from a/3<$11\bar{2}0$> Burgers vectors. In (b) the ($11\bar{2}\bar{2}$) has been allowed to contribute to the image and strong dislocation loop contrast is evident ($\underline{z}$ = [$\bar{1}100$]; 200 kV). In this material the dislocation loop density is extremely high.

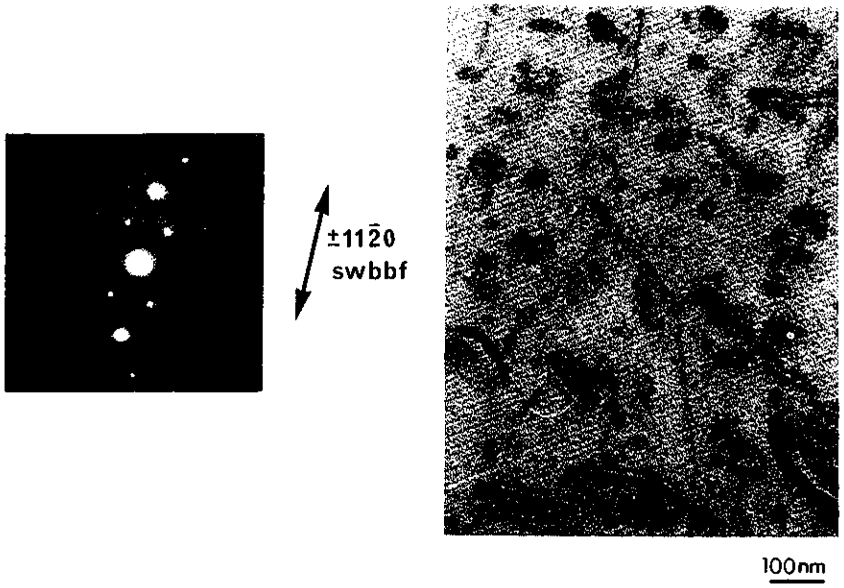

FIGURE 8   MATERIAL AS IN FIGURE 7 IMAGED IN SWBBF WITH $\underline{g}$ = ±($11\bar{2}0$) ($\underline{z}$ ≈ [0001]; 200 kV). DISLOCATIONS AND LOOPS SHOWING DOUBLE IMAGES HAVE $\underline{g}.\underline{b}$ = 2, WHEREAS THOSE WITH $\underline{g}.\underline{b}$ = 1 SHOW FAINTER SINGLE IMAGES.

FIGURE 9   LOOP PLANE NORMALS FOR ZONE REFINED ZIRCONIUM IRRADIATED AT 668 K (395°C) TO 6.4×10^{23} neutrons m^{-2} (> 1 MeV).

The loop Burgers vector has been taken to be a/3[$11\bar{2}0$] and all the results are plotted in a single triangle of the stereographic projection. Vacancy loops are represented by open circles and interstitial loops by full circles.

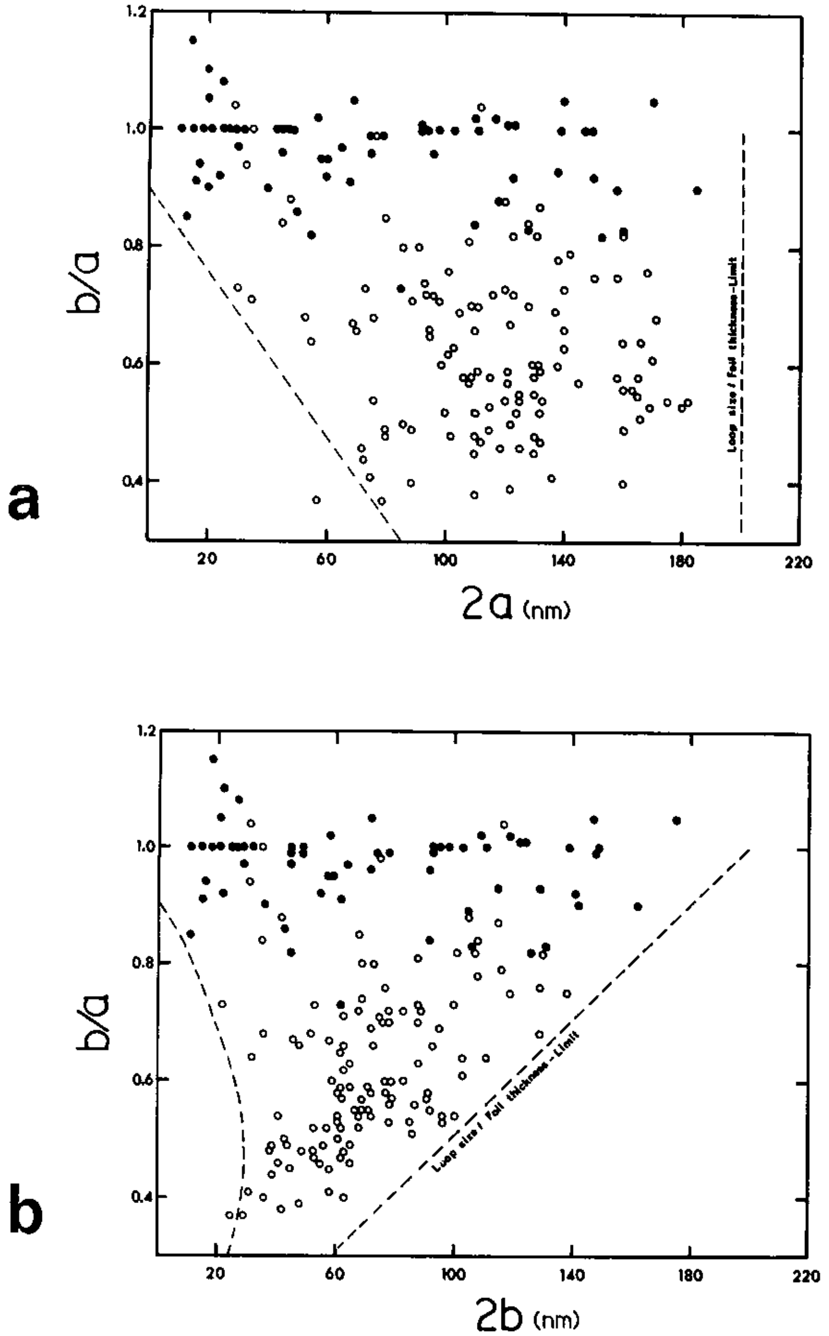

FIGURE 10 ELLIPTICITY VALUES (b/a) AS A FUNCTION OF LOOP SIZE FOR ZONE REFINED ZIRCONIUM IRRADIATED AT 668 K (395°C) TO 6.4 x 10^{23} neutrons m^{-2} (> 1 MeV).

In (a) the loop size is expressed as the major axis dimension 2a and there is a marked cut-off in size at about 200 nm, which corresponds to the foil thickness. In (b) where the size is expressed in terms of the loop minor axis 2b, this cut-off appears as a sloping line and the very elliptical loops appear to cluster over a narrow size range. Note that in both (a) and (b) the interstitial loops are approximately circular while the vacancy loops are elliptical.

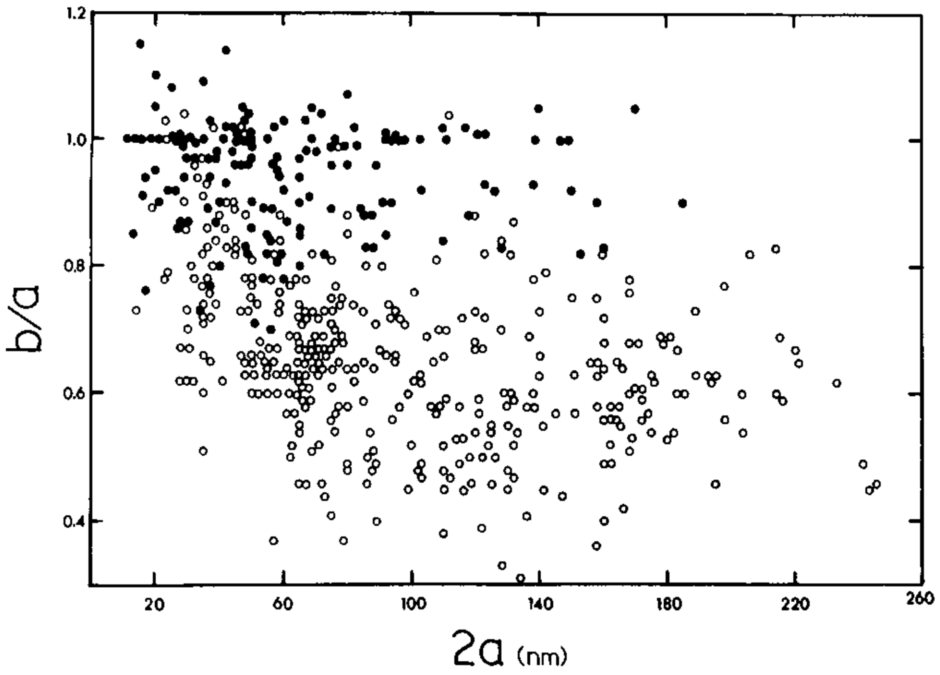

FIGURE 11 LOOP ELLIPTICITY VALUES AS A FUNCTION OF LOOP MAJOR AXIS 2a FOR A SERIES OF SPECIMENS IRRADIATED AT 668 K (395°C) TO FLUENCES FROM 3.3 TO 6.4 x 10^{23} neutrons m^{-2} (> 1 MeV).

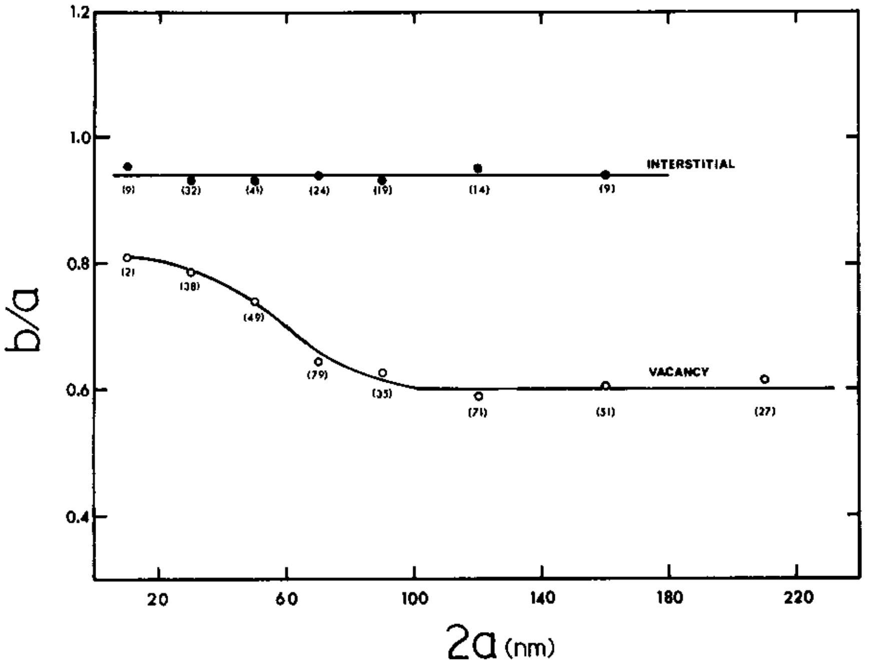

FIGURE 12 AVERAGE VALUES OF LOOP ELLIPTICITY FOR THE LOOPS SHOWN IN FIGURE 11. THE NUMBERS IN BRACKETS REPRESENT THE NUMBER OF LOOPS AVERAGED IN EACH SIZE INTERVAL.

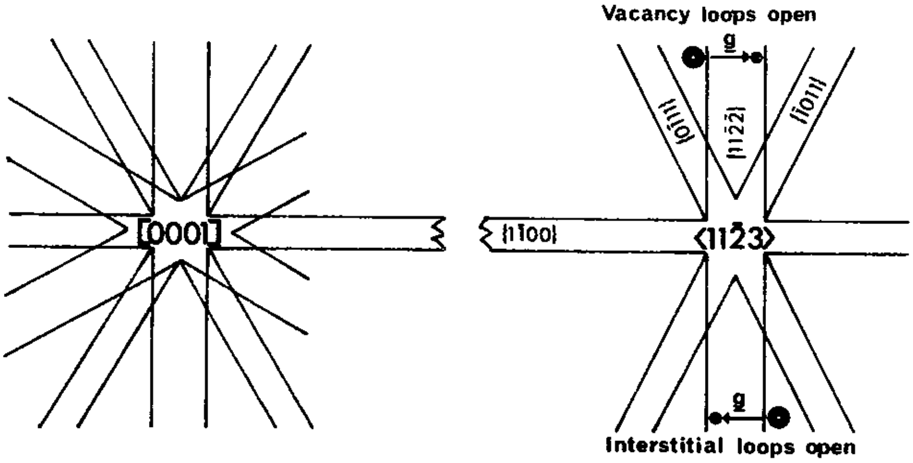

FIGURE 13 KIKUCHI MAP, AS SEEN ON THE MICROSCOPE SCREEN, SHOWING THE SENSE OF $\underline{g}$ = ± (11$\bar{2}\bar{2}$) FOR LOOP CHARACTERISATION NEAR THE SAFE ORIENTATION [11$\bar{2}$3].

FIGURE 14 SAME FIELD AS FIGURE 6, BUT WITH $\underline{z} \approx [1\bar{2}13]$.

In (a), $(\bar{1}2\bar{1}2)$ points away from (0001) (see Figure 6(k)) and hence from Figure 13, loops in outside contrast are vacancy in character. Conversely, the loops in outside contrast in (b) are interstitial. Note the large image shifts associated with the $\underline{g}.\underline{b} = 2$ loops 4, 5, 13 and 14 compared with the smaller shift for $\underline{g}.\underline{b} = 1$ loops 3, 10 and 15. The latter set of loops is interstitial whereas the former is vacancy.

Loop 12 is a good example of the behaviour of weak $\underline{g}.\underline{b} = 1$ images with reversal of $\underline{g}$ — compare (a) with (b). The effect of ω variations with the same $\underline{g}$ is shown by loops 1, 2 and 11 in Figures (b), (c) and (d). At small values of ω the loop contrast is increased, but this is smothered by the enhanced oxide contrast (Figure (d); 200 kV)

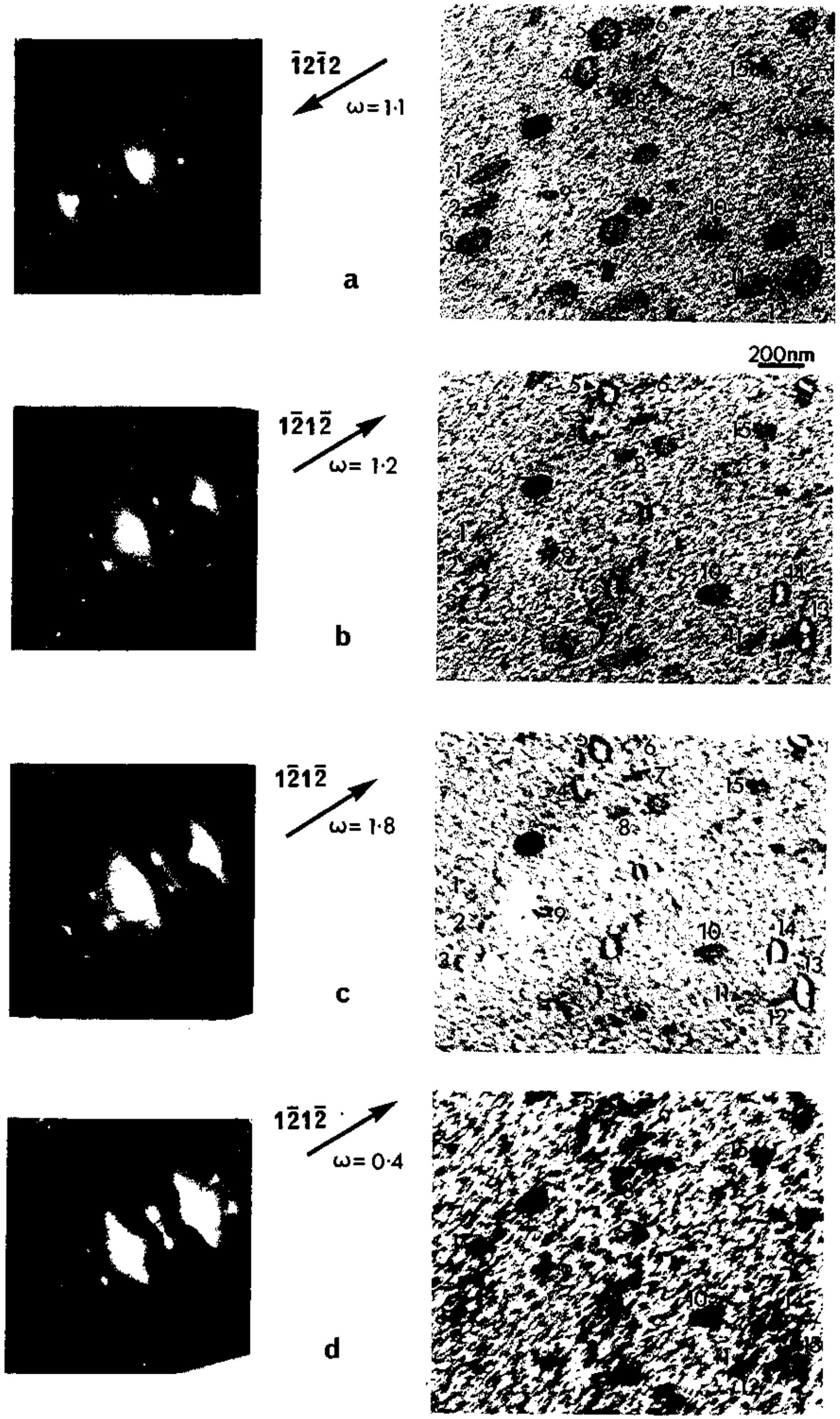

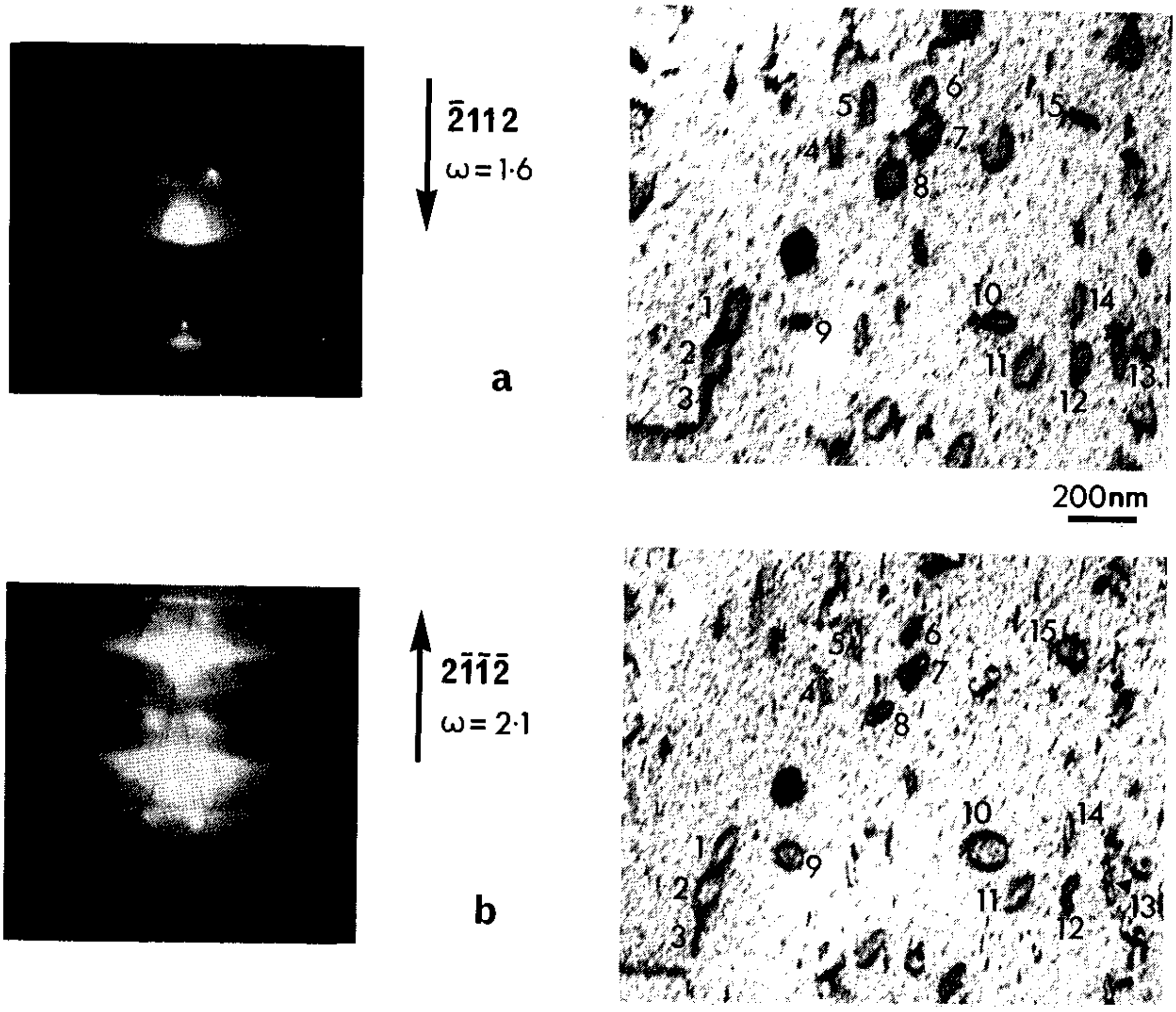

FIGURE 15 SAME FIELD AS FIGURES 6 AND 14, BUT WITH $\underline{z} \simeq [2\bar{1}\bar{1}3]$.

Loops 6, 7, 8 and 11 that were 'unsafe' in Figure 14 are now in a 'safe' orientation. Loops 9, 10 and 15 which gave small image shifts associated with $\underline{g}.\underline{b} = 1$ in Figure 14 now satisfy the condition $\underline{g}.\underline{b} = 2$ and exhibit large image shifts. Loops in outside contrast in (a) are vacancy and in (b) are interstitial (200 kV).

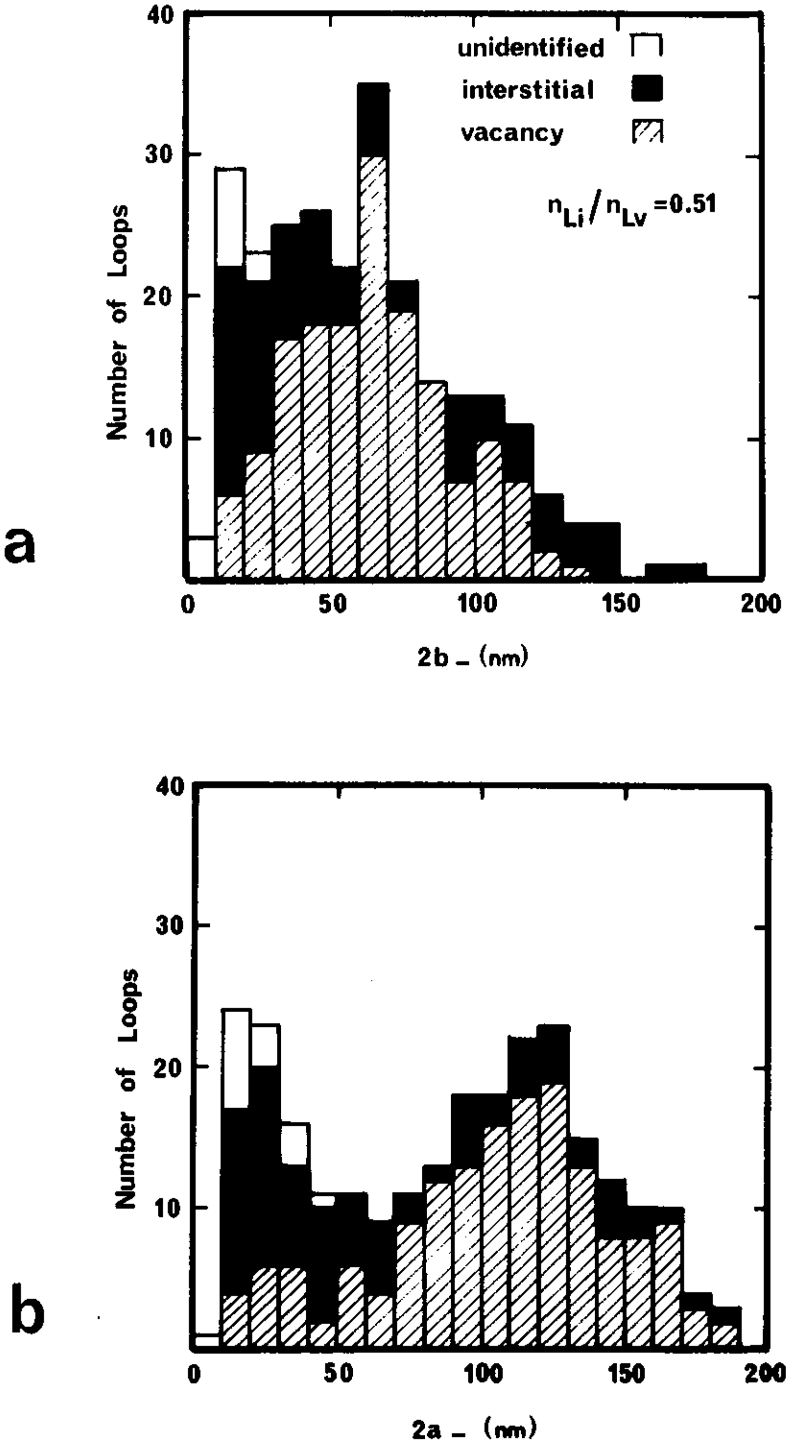

FIGURE 16 SIZE DISTRIBUTION PLOTS FOR 261 LOOPS IN ONE AREA OF A FOIL OF ZIRCONIUM IRRADIATED AT 668 K (395°C) TO 6.4 x 10^{23} neutrons m^{-2} (> 1 MeV).

Note the differences in the shape of the distributions plotted as a function of 2a compared with 2b. The interstitial to vacancy loop ratio in this field is 0.51.

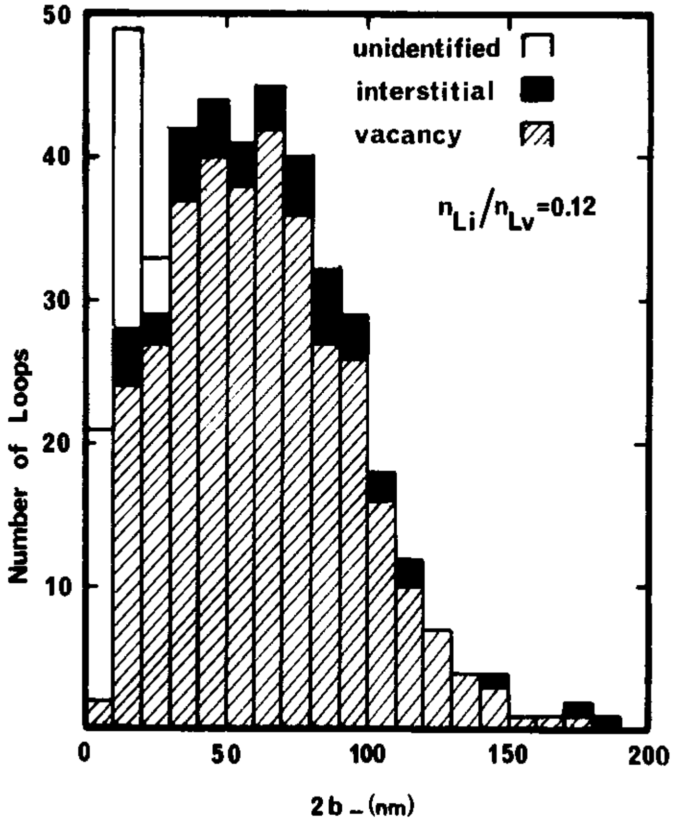

FIGURE 17 SIZE DISTRIBUTION PLOT FOR 426 LOOPS TAKEN FROM THE SAME SPECIMEN USED FOR FIGURE 16, BUT FROM ANOTHER GRAIN

Note that the interstitial to vacancy loop ratio is now 0.12, which is significantly different from the value of 0.51 obtained in the area used for Figure 16.

APPENDIX A

THE EFFECT OF LOOP ELLIPTICITY ON THE ACCURACY OF LOOP NORMAL DETERMINATIONS FROM TRACE ANALYSIS IN THIN FOILS

Conventional trace analysis of a planar feature that intersects a polished surface relies on the knowledge that the observed trace is perpendicular to the normal to the feature being examined. It is this fundamental point which makes trace analysis possible, since it ensures that the locus of normals to the image trace will pass through the normal to the planar feature $\underline{n}$. This point must not be overlooked when trace analysis is applied to planar features embedded in a thin foil being examined by transmission electron microscopy. Admittedly, for a feature such as a perfectly circular loop, this condition is still obeyed. In general, the image of a circular loop will appear as an ellipse, and the long direction of this ellipse will be perpendicular to both the electron beam $\underline{z}$ and the normal $\underline{n}$. The locus of possible plane normals corresponding to this long direction trace will therefore pass through the loop plane normal $\underline{n}$.

Elliptical loops, on the other hand, will not satisfy the condition that the apparent image trace is invariably perpendicular to $\underline{n}$, and this can introduce significant errors in the trace analysis of such a loop. This situation is illustrated in Figure A1, where:

$\underline{z}$ is the direction antiparallel to the electron beam (i.e. $+\underline{z}$ represents the image plane normal pointing UP towards the electron gun;

$\underline{n}$ is the loop plane normal;

$\underline{a}$ is the elliptical loop major axis direction;

$\underline{z} \times \underline{n}$ is the direction in the loop which lies in the image plane and is therefore perpendicular to $\underline{z}$;

$\underline{M}$ is the direction in the loop which projects onto the image plane as the maximum loop image dimension $\underline{M}_z$ (i.e. $\underline{M}_z$ is the major axis of the loop image);

α is the angle between $\underline{z}$ and $\underline{n}$;

ϕ is the angle between $\underline{a}$ and $\underline{z} \times \underline{n}$;

θ is the angle between $\underline{a}$ and $\underline{M}$;

β is the angle between $\underline{M}_z$ and $\underline{z} \times \underline{n}$;

γ is the angle between $\underline{M}$ and $\underline{M}_z$; and

δ is the minimum angle between $\underline{n}$ and the locus of the normal to the image trace $\underline{M}_z$.

The important difference between circular and elliptical loops in a thin foil is that, in the latter case, the image trace $\underline{M}_z$ is not coincident with $\underline{z} \times \underline{n}$. The error introduced by this non-coincidence is a function of the loop ellipticity, expressed as the ratio of the elliptical loop semi-axes (b/a), and the orientation of the loop relative to the electron beam, as defined by the angles α and ϕ. Apart from the circular loop case (b/a = 1), the only time that $\underline{M}_z$ and $\underline{z} \times \underline{n}$ will coincide is when $\phi = 0$ or $\alpha = 90°$. The possible errors can be computed as a function of α and ϕ for a fixed value of b/a. This will define orientations of the foil (i.e. relationships between $\underline{z}$, $\underline{n}$ and $\underline{a}$) where the trace analysis errors will be as small as possible for a particular loop normal $\underline{n}$.

To simplify the calculation, two assumptions have been made:

(i) The elliptical loop image observed on the micrograph really represents the projection of the loop on the image plane. This assumes that there is no 'skewing' of the image, because the diffracting vector $\underline{g}$ is inclined to the long direction of the image, and that there is no inside/outside contrast effect. For small loops imaged under normal conditions, this assumption is not valid. However, for large loops (> 30 nm in size) or in Symmetric Weak Beam Bright Field (SWBBF) micrographs, this assumption is reasonable.

(ii) Only the minimum error from a single trace is computed. As shown in Figure A1, the single locus of the normal to the image trace does not define the normal and a second intersecting locus is required. If the first locus does not pass through $\underline{n}$ as illustrated in Figure A1, the total error will depend on where the second locus intersects the first. In this calculation, it is assumed that the second locus is both perpendicular to the first and passes through $\underline{n}$. Hence, the results given are merely minimum error estimates based on an accurate second trace. In practice, both traces could well be in error and the total discrepancy would then be much greater than the calculated minimum value.

For an ellipse of semi-axes $\underline{a}$ and $\underline{b}$, the length of the radius vector $\underline{R}$ inclined at an angle θ to the major axis $\underline{a}$ is given by:

$$|\underline{R}| = b\left[(b/a)^2\cos^2\theta + \sin^2\theta\right]^{-\frac{1}{2}} \qquad \text{...(A1)}$$

or, in units of b,

$$R_{(b)} = \left[(b/a)^2\cos^2\theta + \sin^2\theta\right]^{-\frac{1}{2}} . \qquad \text{...(A1a)}$$

If this radius vector is inclined at angle γ to the image plane, the projected length R_z in the image will be:

$$R_z = R_{(b)}\cos\gamma = \cos\gamma\left[(b/a)^2\cos^2\theta + \sin^2\theta\right]^{-\frac{1}{2}} . \qquad \text{...(A2)}$$

If this is to correspond to the major axis of the elliptical image (i.e. $R_z \equiv M_z$) then we require the maximum value of R_z (i.e. $R_{z/max}$).

From the Napierian triangle $\underline{M}_z$, $\underline{M}$, $\underline{z} \times \underline{n}$ in Figure A1, we have:

$$\sin\gamma = \sin\alpha \sin(\theta + \phi)$$

i.e.
$$\cos\gamma = \left[1 - \sin^2\alpha \sin^2(\theta + \phi)\right]^{\frac{1}{2}} \qquad \ldots(\mathrm{A3})$$

Combining Equations (A2) and (A3) for maximum R_z (i.e. $R_z \equiv M_z$) we have:

$$R_{z/\max} = M_z = \left[\frac{1 - \sin^2\alpha \sin^2(\theta + \phi)}{(b/a)^2\cos^2\theta + \sin^2\theta}\right]^{\frac{1}{2}}_{\max} \quad . \qquad \ldots(\mathrm{A4})$$

Taking (b/a) = 0.5, for example, it is possible to calculate the maximum value of Equation (A4) for various values of α and ϕ. This gives the value of θ at which R_z is a maximum (i.e. $\theta_{\max}$).

Now, from the Napierian triangle $\underline{z}$, $\underline{n}$, $\underline{x}$ (Figure A1), the value of δ, the minimum trace error, can be given by:

$$\sin\delta = \sin\alpha \sin\beta_{\max} \quad , \qquad \ldots(\mathrm{A5})$$

where $\beta_{\max}$ is the value of β corresponding to $\theta_{\max}$.

From the Napierian triangle $\underline{M}_z$, $\underline{M}$, $\underline{z} \times \underline{n}$:

$$\tan\beta_{\max} = \cos\alpha \tan(\theta_{\max} + \phi) \quad . \qquad \ldots(\mathrm{A6})$$

Combining Equations (A5) and (A6) gives:

$$\delta = \sin^{-1}\left\{\sin\alpha \sin\left[\tan^{-1} \langle\cos\alpha \tan(\theta_{\max} + \phi)\rangle\right]\right\} \quad . \qquad \ldots(\mathrm{A7})$$

The values of δ calculated from Equation (A7) for (b/a) = 0.5 are shown in Figure A2 as contours of constant δ for varying positions of $\underline{z}$, relative to a fixed $\underline{a}$ and $\underline{n}$. For loops with major axis $\underline{a}$ exactly parallel to [0001], a transparent copy of Figure A2 can be laid over a standard projection and then rotated to correspond with the experimentally determined position of $\underline{n}$ to establish whether the foil is in an area of potentially low error or not. In the more usual case, where $\underline{n}$ is not exactly perpendicular to [0001], the projection showing contours of constant δ must first be rotated so that $\underline{n}$ is at the appropriate angle to [0001] before the transparency is laid over a standard projection. The set of δ contours for a loop with $\underline{n}$ inclined at 80° to [0001] is shown in Figure A3. Since $\underline{a}$ can no longer be taken as parallel to [0001] for this position of $\underline{n}$, it has been assumed that the minor axis of the elliptical loop lies in the basal plane, and that the loop major axis $\underline{a}$ is given by the projection of [0001] onto the loop plane. All the experimental evidence available on the shape of loops in irradiated zirconium indicates that this is correct, i.e. the loop minor axis always lies in the basal plane. This assumption is supported by the agreement between theoretical predictions and the experimental loop normal loci, shown in Figure A5.

The experimental observation that the loop plane normals $\underline{n}$ are usually inclined at between 75° and 90° to the [0001] direction means that, for the majority of cases, either Figure A2 or Figure A3 will provide a reasonable estimate of possible trace errors. For example, if Figure A3 is superimposed on a standard [0001] projection of zirconium with $\underline{n}$ in a typical loop habit plane position to give Figure A4, it is obvious that in certain orientations, such as $[\bar{1}\bar{1}23]$, $[\bar{2}113]$, $[11\bar{2}3]$ and $[2\bar{1}\bar{1}3]$, the error will be very large, whereas in other orientations, such as $[1\bar{2}13]$, [0001], $[0\bar{1}10]$, $[1\bar{2}10]$ and $[1\bar{1}00]$, the errors will be insignificant. If two orientations 90° apart are to be selected for loop plane normal determinations, then the basal orientation [0001] and a prism orientation such as $[1\bar{1}00]$ would be the best choices. Even with these two orientations, all the loops cannot be analysed with the same accuracy, and the errors will be somewhat greater for loops whose normals lie close to the chosen $<1\bar{1}00>$ prism axis.

An example which clearly illustrates the errors in the trace analysis of elliptical loops is given in Figure A5. The loop in question was a large vacancy loop (No. 3 in Figure 6) with b/a = 0.45 and 2b = 105 nm. Trace analysis was carried out in four different orientations — one close to a $<10\bar{1}0>$ orientation labelled A, one close to the basal orientation labelled C, and two different $<11\bar{2}3>$ orientations labelled B and D. Figure A4 shows that the prism and basal orientations should be relatively immune from ellipticity errors, so the habit plane normal $\underline{n}$ can be taken to be the point A/C, which corresponds to the intersection of the loci of the normals to the traces in these two orientations. Knowing that this position for $\underline{n}$ is relatively accurate (say within ± 3°), the stereographic projection of Figure A5 has been oriented to correspond with Figure A4, which gives the trace errors for loops with b/a = 0.5.

Comparison of these two figures shows that orientation B would be close to $[2\bar{1}\bar{1}3]$ of Figure A4 and so should produce a trace which is in error by about 30°. The normal locus for this orientation is shown as a dotted line on Figure A5 and, as expected, is completely inconsistent with the correct loop normal $\underline{n}$. In fact, its minimum angular distance from $\underline{n}$ (i.e. the experimental value of δ) is 28°, which is in excellent agreement with the predicted theoretical δ value of 30°. The predicted normal locus for the loop in orientation B can be computed and is shown as a full line in Figure A5. Again, the agreement between theory and experiment is remarkably good.

Orientation D is also of the type $<11\bar{2}3>$, and corresponds to $[1\bar{2}13]$ in Figure A4. Hence the normal locus for this trace should be reasonably accurate and, as Figure A5 shows, this is the case.

Another important point illustrated by the example in Figure A5 is that although the *minimum* error δ for orientation B is about 30°, this situation will only arise if the second normal locus intersects the normal locus for B at right angles. For intersection angles less than 90°, the inaccurate loop plane normal will be more than 30° away from the true position at $\underline{n}$. Thus, the intersection of normal loci from orientations A and B (the point A/B) is 32° from $\underline{n}$, B/C is 36° from $\underline{n}$ and, worst of all, B/D is 76° from $\underline{n}$. In the absence of other information, the results obtained from any of these isolated pairs of orientations AB, BC and BD could have been used to determine the loop plane normal and they would all have been wrong — one of them (B/D) would have been particularly inaccurate.

The result produced by orientations B and D is not potentially the most dangerous case, since it would almost certainly have been recognised as conflicting with other data. Result A/B on the other hand appears quite reasonable. For a loop with an a/3 $\langle 11\bar{2}0 \rangle$ Burgers vector in the position shown by the arrow in Figure A5, the loop plane normal A/B is just as likely as $\underline{n}$. Had this particular loop been analysed at orientations A and B in the first instance, there would be no reason to suspect the result as being incorrect. Even if loop ellipticity had been taken into account and Figure A5, with $\underline{n}$ transferred to the position A/B, had been manipulated into the orientation of Figure A4, it would have appeared that orientation B was in the relatively safe position corresponding to $[\bar{1}2\bar{1}3]$. This would predict a minimum error of about 10°, and could have been regarded as adequate. However, a confirmatory third trace from an inherently more accurate orientation such as C would have immediately shattered the calm of scientific complacency.

The moral of this is that in determining the habit plane normals of elliptical loops in zirconium it is better to avoid using any orientations other than the prism and the basal orientations. Admittedly, this means that the thin foil has to be tilted by 90° from prism to basal, but this is the ONLY way to ensure that the loop plane normal results are correct. Although particular $\langle 11\bar{2}3 \rangle$ orientations may be acceptable for certain loops, there is no way of ensuring, without prior knowledge of the loop normal position, that an appropriate $\langle 11\bar{2}3 \rangle$ orientation has been selected.

Another piece of information which comes from this calculation of trace analysis errors for elliptical loops is an estimate of the accuracy of loop dimension measurements. Apart from normal measurement errors, which are more significant in the case of small loops, it is apparent that the best value for the loop major axis dimension will be obtained from foils oriented so that the major axis in question is nearly perpendicular to the beam, i.e. in a prism orientation. Similarly the best loop minor axis dimension will be obtained from basal oriented foils, since the minor axis lies in the basal plane. This can be quantified by examining the errors in loop semi-axis dimensions for different orientations of the foil, i.e. by comparing $R_{z/max}$ of Equation (A4) with either a or b. This has been done for loops with $b/a = 0.5$ in the two orientations used in Figures A2 and A3. The results are shown in Figures A6 and A7. Note that the loop major axis is always underestimated at orientations removed from the prism positions, while the minor axis is always overestimated as the foil departs from the [0001] orientation. However, these figures do show that these dimensional errors are never severe, provided the measurements are made close to the prism and basal orientations.

Finally, it is worth noting that all the errors discussed in this Appendix are a function of the loop ellipticity. As the value of b/a approaches unity (i.e. the loops become more circular), the errors decrease to zero. Conversely, very elliptical loops ($b/a < 0.5$) give very large errors, particularly in trace analysis.

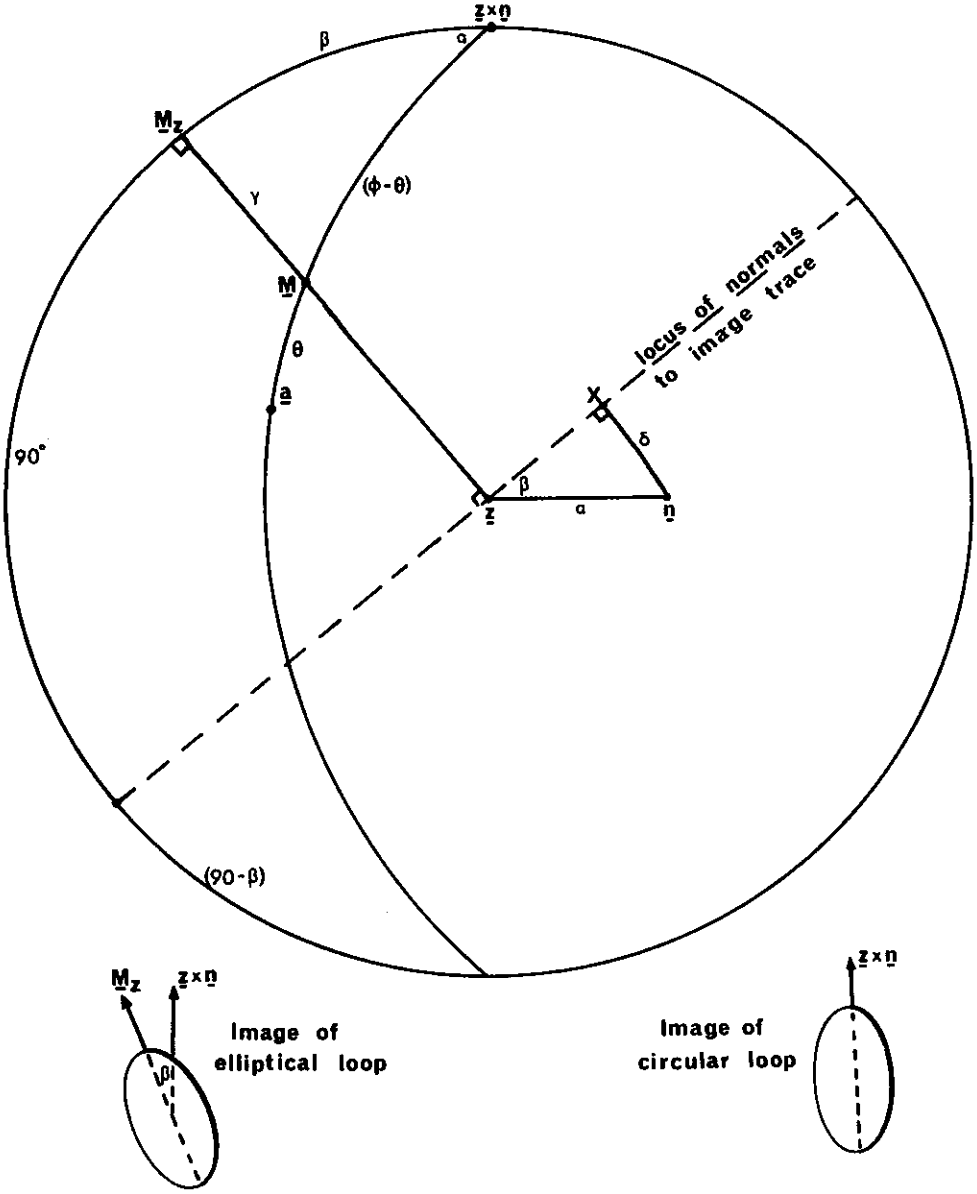

FIGURE A1 STEREOGRAPHIC PROJECTION ILLUSTRATING THE GEOMETRY ASSOCIATED WITH TRACE ANALYSIS OF ELLIPTICAL LOOPS

Direction $\underline{M}$ in the loop projects at $\underline{M}_Z$, the loop *image* major axis, and errors resulting from non-parallelism of $\underline{M}_Z$ and $\underline{z} \times \underline{n}$ produce a minimum loop plane normal error δ.

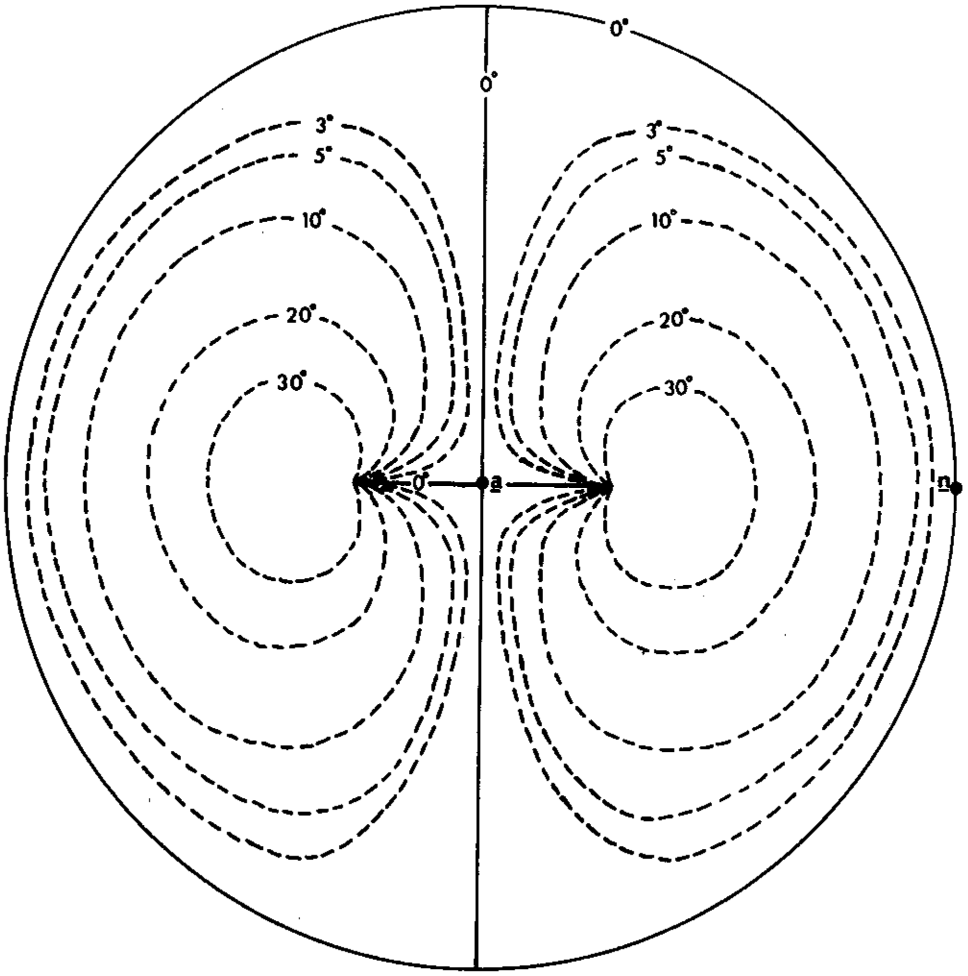

Trace error b/a = 0.5

FIGURE A2 STEREOGRAPHIC PROJECTION SHOWING CONTOURS OF CONSTANT MINIMUM ERROR δ AS A FUNCTION OF FOIL ORIENTATION FOR LOOPS WITH ELLIPTICITY b/a = 0.5.

The centre of the projection corresponds to [0001], the loop plane normal n lies in the basal plane and the loop major axis a is parallel to [000$\bar{1}$].

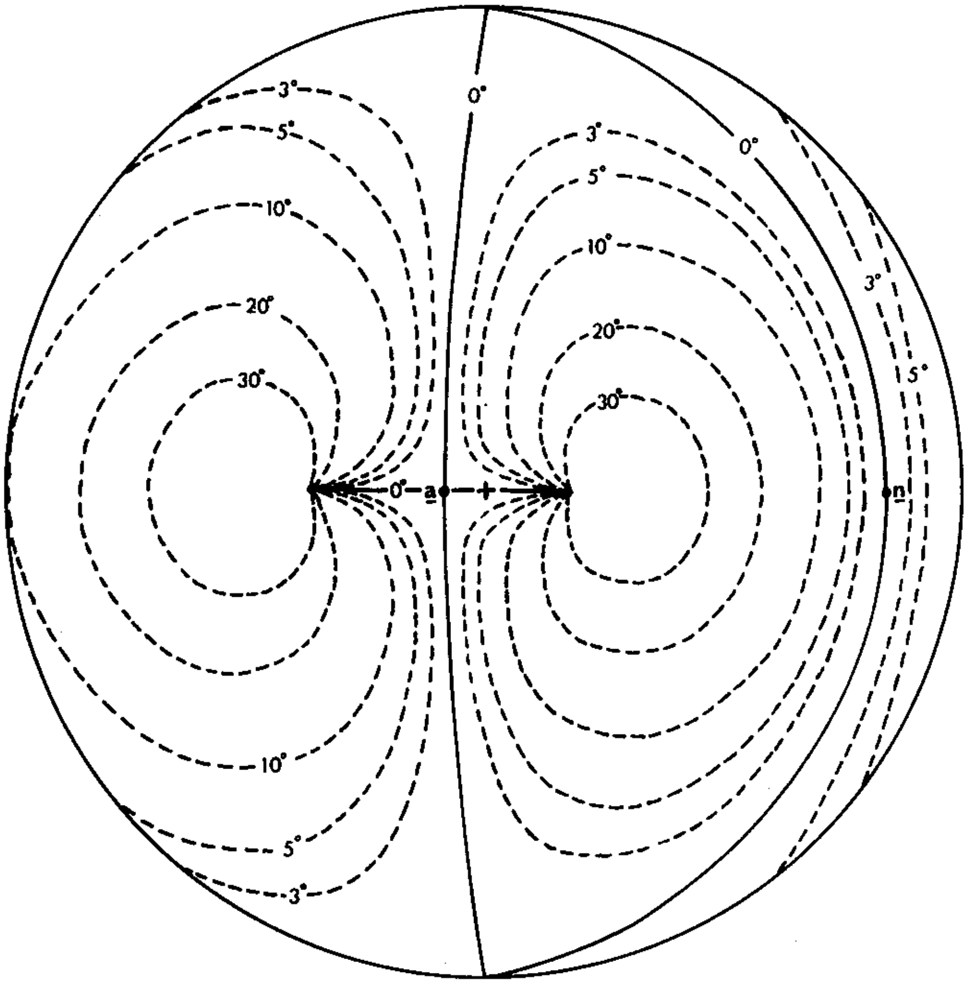

Trace error b/a = 0.5

FIGURE A3 AS FIGURE A2, BUT ROTATED 10° ABOUT $\underline{a}$ × $\underline{n}$.

The loop minor axis $\underline{b}$ is assumed to lie in the basal plane so that the major axis $\underline{a}$ is given by the projection of [0001] on the loop plane.

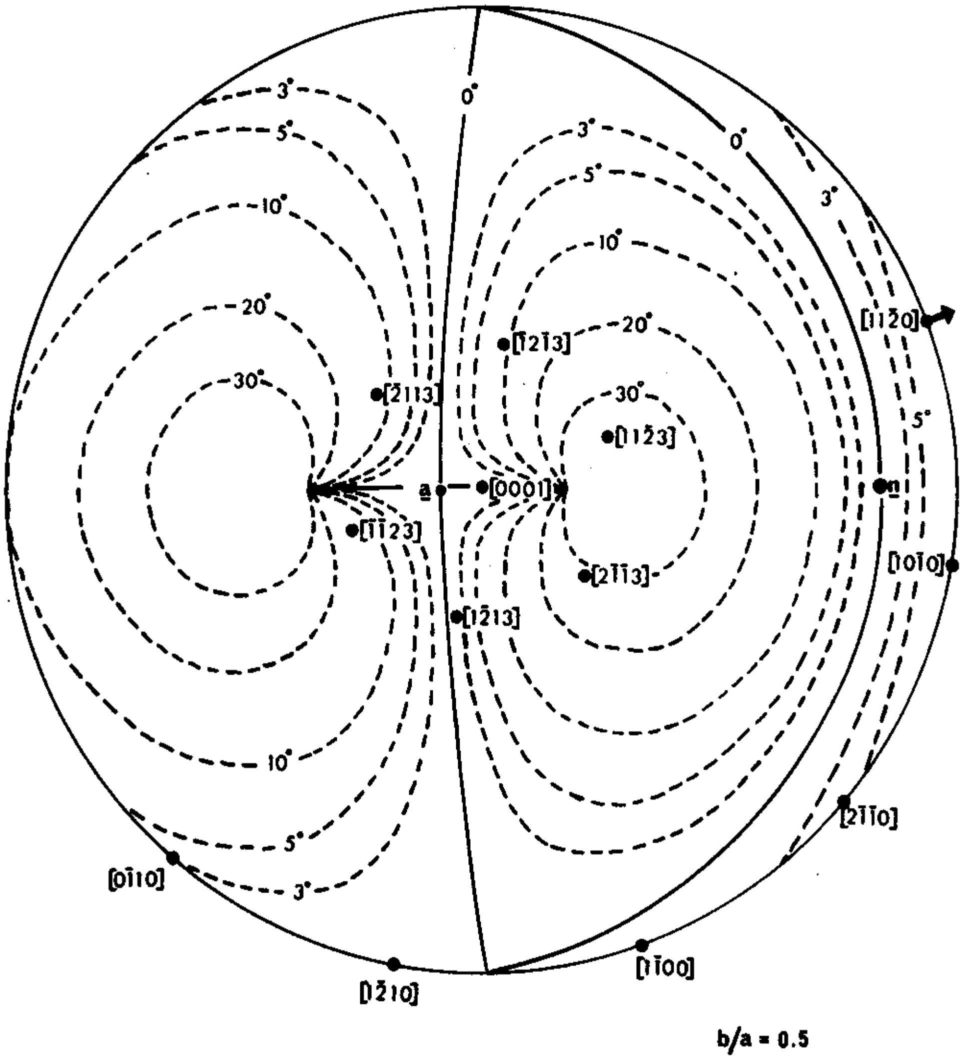

FIGURE A4 CONTOURS OF FIGURE A3 SUPERIMPOSED ON A STANDARD PROJECTION OF DIRECTIONS IN ZIRCONIUM.

The loop plane normal has been placed in a position corresponding to the observed normals for loops with Burgers vector a/3 $[11\bar{2}0]$. Note that, to ensure that errors are kept to a minimum, the loop plane normals should be determined in basal or prism orientations. Any other orientation is potentially open to error.

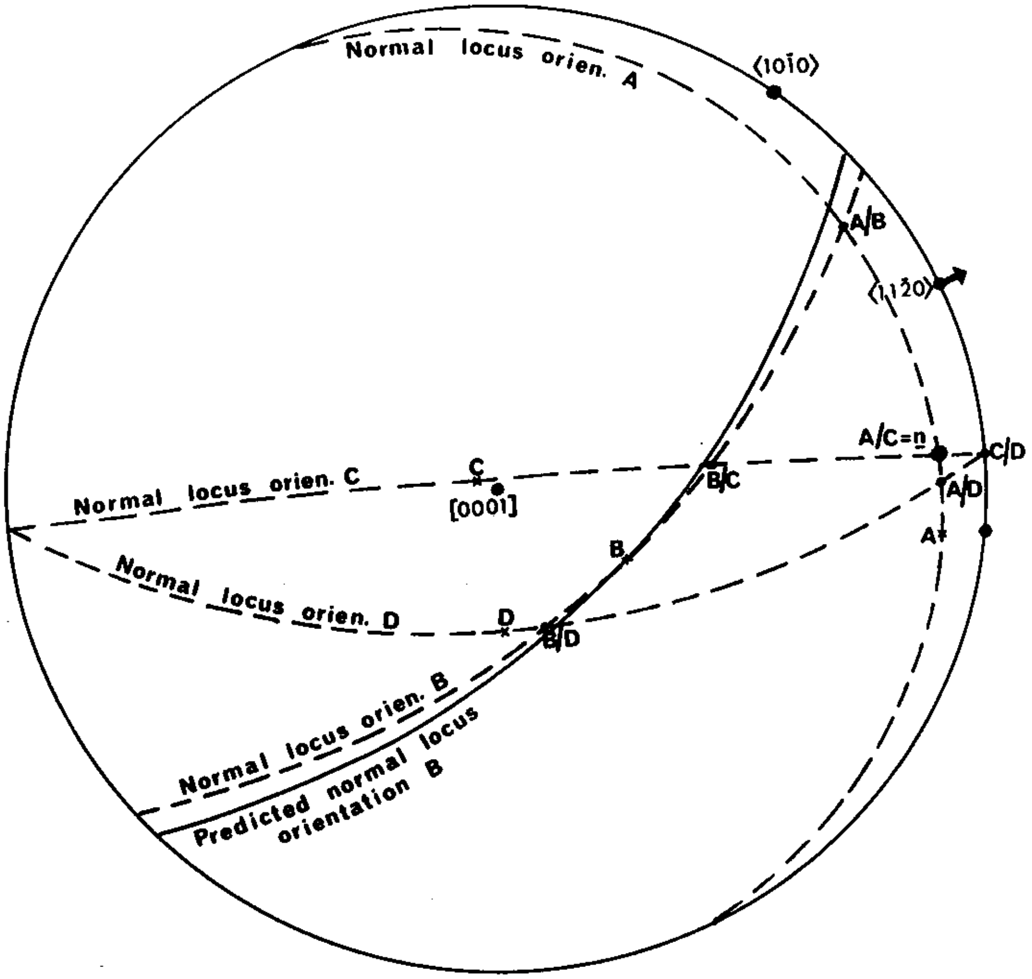

FIGURE A5 LOOP PLANE NORMAL ANALYSIS FOR LOOP 3 OF FIGURE 6, SHOWING THE LARGE ERRORS THAT RESULTED FROM USING THE <11$\bar{2}$3> ORIENTATION LABELLED B.

The three normals that involved traces from this orientation (A/B, B/C and B/D) are in error by 32 to 76°. The prism and basal orientations A and C give a loop normal position, which Figure A4 predicts should be accurate to ± 3°.

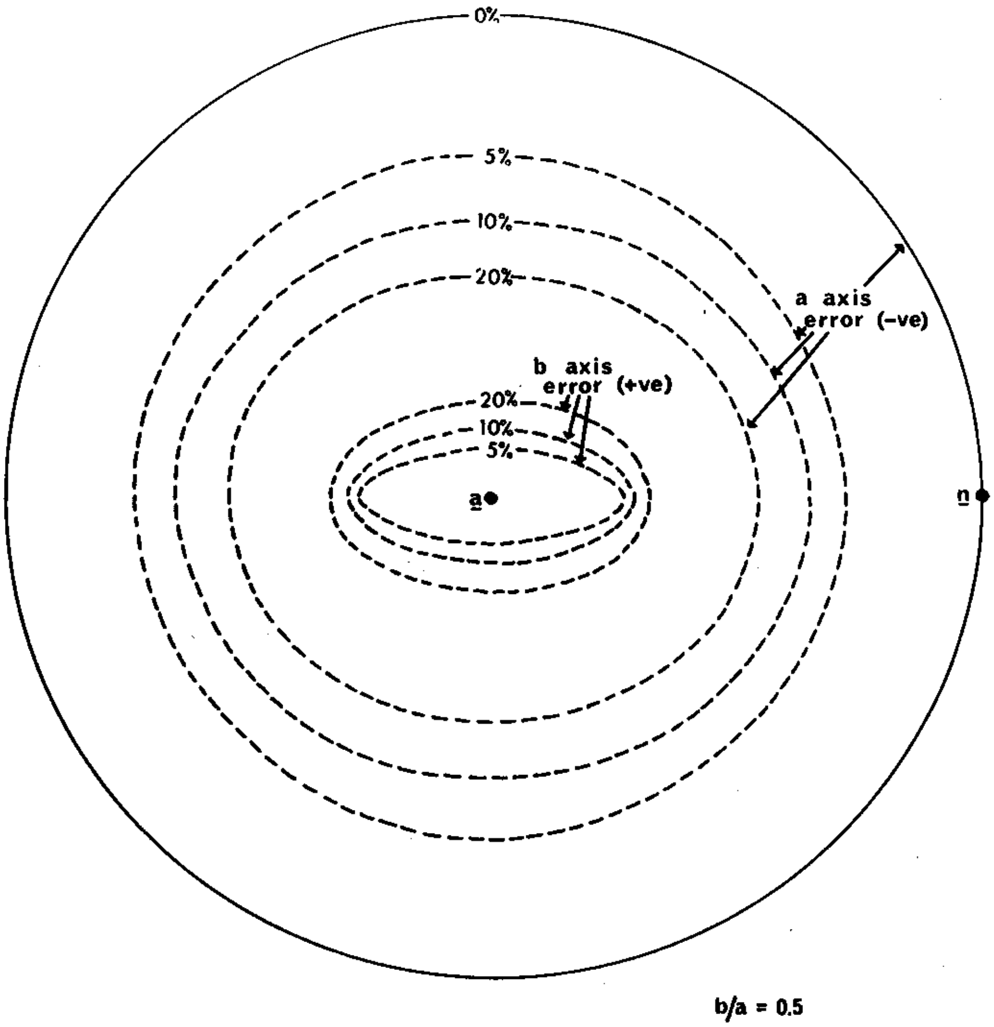

FIGURE A6 STEREOGRAPHIC PROJECTION CENTRED ON [0001] SHOWING CONTOURS OF CONSTANT ERROR IN MEASUREMENTS OF ELLIPTICAL LOOP SEMI-AXES AS A FUNCTION OF FOIL ORIENTATION.

The loop ellipticity is 0.5, the loop plane normal lies in the basal plane and the loop major axis a̲ is parallel to [0001]. Note that the b̲ axis error is always positive (i.e. the b̲ axis measurement is an overestimate) while the a̲ axis error is always negative. By restricting measurements to basal or prism orientations, the errors will be less than 1 or 2%.

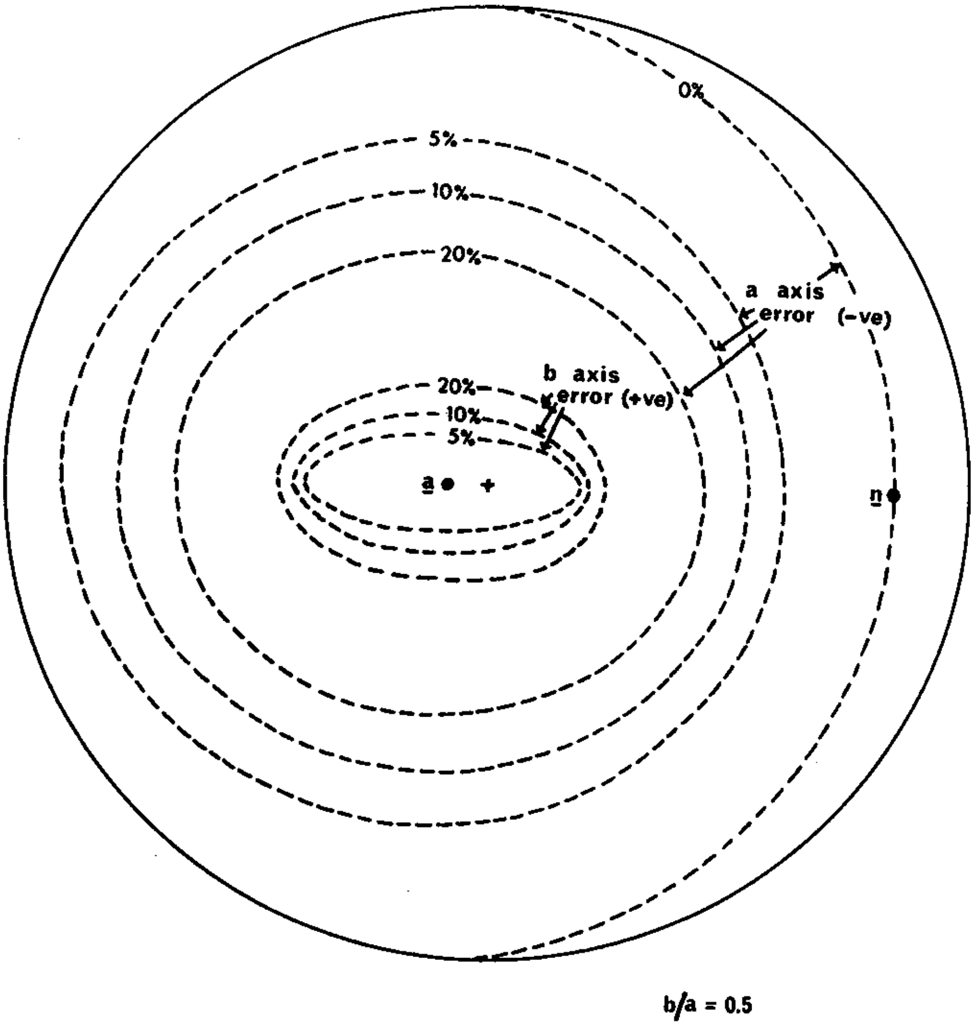

FIGURE A7 AS FIGURE A6, BUT ROTATED 10° ABOUT a × n.

The loop minor axis is assumed to lie in the basal plane as in Figure A3.

APPENDIX B

NOMENCLATURE

$\underline{a}$	The close packed direction $<11\bar{2}0>$ in a hexagonal crystal. (Also used in Appendix A to specify the elliptical loop major axis direction.)
2a	Elliptical loop major axis
2b	Elliptical loop minor axis
$\underline{b}$	Burgers vector of a dislocation loop
$\underline{c}$	The axis [0001] in a hexagonal crystal
$\underline{n}$	Loop plane normal. (By convention $\underline{n}$ always points upwards towards the electron gun.)
$\underline{u}$	Direction of a dislocation line
$\underline{z}$	Direction antiparallel to the electron beam (+$\underline{z}$ represents the image plane normal pointing UP towards the electron gun)
$\underline{g}$	Operating reflection
s	Deviation from the exact Bragg position
ξ_g	Extinction thickness

$\omega = s\xi_g$